

DOI: 10.1002/ ((please add manuscript number))

Article type: Full Paper

## Long cycle life, low self-discharge sodium-selenium batteries with high selenium loading and suppressed polyselenide shuttling

Hui Wang,<sup>a,b</sup> Yang Jiang,<sup>b,\*</sup> and Arumugam Manthiram<sup>a,\*</sup>

Dr. Hui Wang, Prof. A. Manthiram

<sup>a</sup> Materials Science and Engineering Program & Texas Materials Institute, The University of Texas at Austin, Austin, TX 78712, USA

E-mail: [manth@austin.utexas.edu](mailto:manth@austin.utexas.edu)

Dr. Hui Wang, Prof. Yang Jiang

<sup>b</sup> School of Materials Science and Engineering, Hefei University of Technology, Hefei, Anhui 230009, P. R. China.

E-mail: [apjiang@hfut.edu.cn](mailto:apjiang@hfut.edu.cn)

**Keywords:** sodium-selenium batteries, carbon nanofiber-selenium cathode, high selenium loading, carbon-coated separator, polyselenide shuttle

**Abstract:** The use of selenium as a cathode in rechargeable sodium-selenium batteries is hampered by low Se loading, inferior electrode kinetics, and polyselenide shuttling between the cathode and anode. We present here a high-performance sodium-selenium cell by coupling a binder-free, self-interwoven carbon nanofiber–selenium cathode with a light-weight carbon-coated bifunctional separator. With this strategy, electrodes with a high Se mass loading (4.4 mg cm<sup>-2</sup>) renders high reversible capacities of 599 mA h g<sup>-1</sup> at 0.1C rate and 382 mA h g<sup>-1</sup> at 5C rate. In addition, this novel cell offers good shelf-life with a low self-discharge, retaining 93.4% of its initial capacity even after resting for six months. As evidenced by experimental and density functional theory (DFT) analysis, the remarkable dynamic (cycle life) and static (shelf-life) stabilities originate from the high electrical conductivity, improved Na-ion accessibility through the 3D interconnected open channels, and highly restrained polyselenide shuttle. The results demonstrate the viability of high-performance sodium-selenium batteries with high selenium loading.

## 1. Introduction

Wide-scale integration of renewable energy into the electric grid requires the development of high energy density, low-cost energy storage systems.<sup>[1, 2]</sup> Among the various energy storage systems, state-of-art lithium-ion batteries (LIBs) are the most promising candidates for this application.<sup>[3-5]</sup> However, the ever-increasing demand for LIBs and geographic-restriction of Li precursors impose limitations on the large-scale applications of LIBs.<sup>[6-12]</sup> In contrast, sodium-ion batteries (SIBs) offer an alternative chemistry to LIBs for large-scale energy storage demands due to the wide availability and abundance of sodium.<sup>[9, 13]</sup> In addition, the electrode dynamics and thermodynamic knowledge accrued recently for LIBs could be employed to ensure rapid advances in SIBs.<sup>[14-18]</sup> Thus, development of viable room-temperature sodium-ion batteries is attracting increasing attention.<sup>[19-24]</sup>

Recently, room-temperature (RT) sodium-sulfur (Na-S) batteries, based on the conversion reaction chemistry, have triggered extensive research interest due to the high charge-storage capacity and the abundance of both sodium and sulfur.<sup>[25-30]</sup> However, the practical applications of RT Na-S batteries are facing two major challenges: (i) sulfur has a low electronic conductivity ( $5 \times 10^{-30}$  S cm<sup>-1</sup> at 25 °C), thus leading to sluggish electrochemical reaction processes and low utilization of the active sulfur in the electrode; (ii) severe “polysulfide shuttle effect”, *i.e.*, migration of dissolved polysulfide intermediate products through the porous separator between the cathode and the anode, which leads to rapid capacity fade during cycling.<sup>[31]</sup> Many approaches have been pursued to mitigate these issues, including employing modified separators,<sup>[30]</sup> porous carbon matrix,<sup>[26]</sup> etc. However, the intrinsic challenges of RT Na-S batteries have been far from completely solved. Selenium is a chemical analogue of S<sup>[32, 33]</sup> and is considered to be an alternative electrode materials for SIBs due to its much higher electronic conductivity ( $1 \times 10^{-3}$  S m<sup>-1</sup>) as indicated in Figure S1, volumetric capacity (3253 Ah L<sup>-1</sup>) comparable to that of S (3467 Ah L<sup>-1</sup>), and stable function

in the relatively low-cost carbonate-based electrolytes.<sup>[34-36]</sup> However, bulk Se particles still suffer from low active material utilization and coulombic efficiency due to its electronically insulating properties and shuttling of high-order polyselenides. To circumvent these problems, the current efforts are mainly concentrated on improving the electrical conductivity and entrapping the active material within the cathode region, which include microporous/mesoporous carbon-selenium,<sup>[37-39]</sup> slit microporous carbon-selenium,<sup>[34]</sup> and flexible porous carbon nanofiber-selenium.<sup>[40, 41]</sup> With these approaches, the introduction of additional components (such as carbon black and binders) often lowers the energy density of Na-Se batteries. Also, fabrication of these electrodes often involves complex multistep processes.

In light of these pros and cons, we present herein a facile and scalable strategy to design carbon nanofiber (CNF)/selenium composites with high loading, good dynamic (cycle life) and static (shelf-life) stability, and excellent electrochemical performance by coupling with a light-weight carbon-coated separator. This novel cell is able to yield a highly reversible specific capacity of 599 mA h g<sup>-1</sup> at 0.1C rate and maintains 382 mA h g<sup>-1</sup> at 5C rate (1C = 675 mA g<sup>-1</sup>). Moreover, the battery still retains 93.4% of the initial capacity even after resting for six months. The superior electrochemical performance metrics have evidenced the following advantages of this cell: (i) the highly porous 3D interconnected CNF framework significantly improves electron and Na ion accessibility, thus rendering high power density; (ii) the light-weight carbon-coated layer (0.3 mg cm<sup>-2</sup> according to Figure S2) fabricated with low-cost materials and simple processing techniques suppresses the “shuttle effect” and increases the dynamic (cycle life) and static (shelf-life) performance as illustrated by experimental and DFT results; and (iii) the self-interwoven CNF with optimized micropores and mesopores allows for a high Se loading (72.1 wt. %, 4.4 mg cm<sup>-2</sup> according to Figure S2) for high energy density Na-Se batteries.

## 2. Results and Discussion

As shown in Figure 1a and 1f, the CNF/Se electrodes with a high mass loading (4.4 mg cm<sup>-2</sup>) were fabricated through a facile vacuum-filtration, peel-off, KOH activation, and a Se infiltration process. In parallel, the light-weight carbon coating (0.3 mg cm<sup>-2</sup>) on the separator, functioning as the polyselenide diffusion barrier, was prepared through a facile tape casting method. As illustrated in Figure 1b and 1c, the CNF/Se composites maintain the CNF morphology and no Se particles could be observed on the surfaces of the CNF. Elemental mapping of the CNF/Se verifies the uniform distribution of Se in CNF as demonstrated in Figure 1d and 1e. Decreasing the infiltration temperature from 260 to 230 °C and 110 °C results in clear segregation of Se on the surface of CNF, which can be observed as shown in Figure S3a and S3b. Se aggregation on the CNF results in poor electrochemical performance, as clearly presented in Figure S3c and S3d. Figure 1g, 1h, 1i and 1j shows the field emission scanning electron microscopy (FESEM) images of the pure glass fiber separator cross section, carbon-coated glass fiber cross section, and the porous carbon surface morphology. The carbon-coated side of the glass fiber separator faces the CNF/Se electrode and aims at preventing the free migration of high-order sodium polyselenides through the separator. The uncoated side of the insulating glass fiber remains highly electronically resistive. As evidenced by the much improved electrochemical performance discussed later, it can be recognized that during long-term cycling, the carbon-coated separator not only significantly mitigates the shuttle effect, but also reactivates the active material, thus ensuring high selenium utilization.<sup>[30, 42]</sup>

Figure 2a displays the crystal structure and phase purity of the CNF/Se composite. It was found that all the characteristic peaks of Se in the XRD profiles disappear after the selenation process, implying an elaborate dispersion of amorphous Se into the CNF.<sup>35</sup> As shown in Figure S4a, the Se content in the CNF/Se electrode is high. Selenium loading was

determined to be as high as  $4.4 \text{ mg cm}^{-2}$  (72.1 wt. %) by thermogravimetric analysis (TGA). Raman spectroscopy was then applied to investigate the vibrational characteristics of the CNF/Se composite. As indicated in Figure 2b, the pristine Se displays a sharp peak located at  $234 \text{ cm}^{-1}$ , which corresponds to trigonal Se.<sup>30</sup> However, for CNF/Se, the Se peak intensity is decreased and shifted to around  $260 \text{ cm}^{-1}$ . This corresponds to the transformation from crystalline Se to molecular  $\text{Se}_8$ , in agreement with the simulation results ( $262.7 \text{ cm}^{-1}$ ).<sup>34</sup> The chemical state of Se was further investigated by X-ray photoelectron spectroscopy (XPS) as indicated in Figure 2c and S4b. The 3d peak of Se is split into  $3d_{3/2}$  and  $3d_{5/2}$  with binding energies, respectively, of 56.2 and 55.3 eV. This is slightly higher than the binding energy of common Se/C composites (55.9 and 55.1 eV) as shown in Figure S5a, implying some chemical interaction between Se and CNF matrix. In addition, the interaction between Se and CNF matrix is further verified by some degree of Se-O bonding observed in the Se 3p XPS spectrum (Figure S5b) and by Se-C bending and stretching peaks observed in the FT-IR spectrum (Figure S5c and S5d).<sup>[37]</sup>

To examine the effects of KOH activation, nitrogen adsorption–desorption isotherms of KOH activated CNF and the porous carbon used for the coating were measured at 77 K. As shown in Figure 2d and S4c, the Brunauer–Emmett–Teller (BET) surface area / pore volume of the activated CNF and the porous carbon are, respectively, as high as  $621 / 481 \text{ m}^2 \text{ g}^{-1}$  and  $1.02 / 0.84 \text{ m}^3 \text{ g}^{-1}$ , while the inactivated CNF only shows a low surface area and pore volume of, respectively,  $50 \text{ m}^2 \text{ g}^{-1}$  and  $0.10 \text{ m}^3 \text{ g}^{-1}$  as shown in Figure S4d, S6c, revealing the high chemical activation ability of KOH and ensuring better trapping and accommodation of the cycled products. After the Se impregnation, the BET surface area of the CNF as shown in Figure 2c decreases to  $61 \text{ m}^2 \text{ g}^{-1}$ , together with a remarkable decrease in pore-size distribution in the 1 to 4 nm range as shown in Figure S6a and S6b, implying the diffusion of Se into the pores of the CNF.

Electrochemical performances of the self-interwoven CNF/Se composites were

evaluated with CR2032 coin cells. Figure 3a shows the cyclic voltammograms (CV) of the half cell in the range of 0.5 - 3V at a high scan rate of 0.5 mV s<sup>-1</sup>. In the first sodiation process, a cathodic peak appears at 1.12 V and shifts to 1.29 V after the first cycle, which can be assigned to the electrochemical activation process.<sup>[39, 41, 43]</sup> For the desodiation reaction, it should be noted that the anodic peak remains steady at 1.63 V, thus indicating the effective maintenance of the capacity and suppression of the shuttle.<sup>[34, 41]</sup> Figure 3b demonstrates the initial six discharge-charge profiles of the cell employing the C-coated separator. During the discharge-charge process, the single plateau observed can be related to the conversion of Se<sub>n</sub> to insoluble Na<sub>2</sub>Se.<sup>[37]</sup> This result is consistent with the *ex situ* XRD results (Figure S6d). Figure 3b also shows that the CNF/Se electrode yields initial discharge and charge capacities of, respectively, 814 mA h g<sup>-1</sup> and 599 mA h g<sup>-1</sup>. The irreversible capacity of the initial cycle may be associated with the solid electrolyte film (SEI) formation, together with some irreversible trapping of Na within the bulk carbon and carbon pores, as verified in Figure S7a and 7b.<sup>[38, 41, 44]</sup> To evaluate the cycling performance, the as-fabricated cells were tested at rates of 0.1, 0.2, 0.5, 2 and 5C. As illustrated in Figure 3c, 3d and 3e, the CNF/Se electrodes with carbon-coated separator exhibit excellent capacity retention: a reversible capacity of 512 mA h g<sup>-1</sup> is obtained at 0.1C rate after 120 deep cycles, and 478, 362, 334 mA h g<sup>-1</sup> are obtained after 200 cycles respectively, at 0.5, 2, and 5C rates, corresponding to an enhanced 85.6%, 89.8%, 83.2%, and 87.4% capacity retention and nearly 100% coulombic efficiency. It is noteworthy that the cycling stability at high current rates, even at 5C, is better than that at 0.1C rate. This may be attributed to the following: (i) the highly porous 3D interconnected CNF framework improves significantly the electron and Na-ion accessibility, thus ensuring high electrode reaction kinetics even at high current rates; and (ii) the cycled long-chain products (Na<sub>2</sub>Se<sub>x</sub>) at low current rates have more chance to combine with EC/DMC and dissolve into the electrolyte, increasing the “shuttle effect” and thus weakening the cycling stability.<sup>[25, 34, 45]</sup> By contrast, the capacity of the CNF/Se electrodes with pure glass fiber

separator decreased rapidly from 597 mA h g<sup>-1</sup> to 522 mA h g<sup>-1</sup> during the initial six cycles and only 374 mA h g<sup>-1</sup> is retained after 94 cycles at 0.1Crate as displayed in Figure 3c and S9a, together with much poorer rate performance at 0.1, 0.2, 0.5, 2, 5C rates, which may be attributed to severe polyselenide shuttling.

Electrochemical impedance spectroscopy (EIS), as shown in Figure 4a and 4b, was also utilized to evaluate the stable long-term cycling performance of the CNF/Se electrodes. As clearly seen, compared with the CNF/Se-pure electrode with pure glass fiber separator, the CNF/Se electrode with the modified separator displays a relatively higher reversible electrochemical reaction process. Figure S8 shows the resistance parameters obtained by modeling the experimental impedance. The pristine CNF/Se cell with the C-coated separator delivers an equivalent series resistance (R<sub>el</sub>) of 3.85 Ω and a charge-transfer resistance (R<sub>ct</sub>) of 104.5 Ω. After 10, 30, 50, and 100 cycles, these values increased, respectively, to 5.01, 5.56, 5.58, and 5.65 Ω and 119.2, 131.4, 136.2, 152.8 Ω. By contrast, the cell with CNF/Se with a pure glass fiber separator shows much larger R<sub>el</sub> (5, 11.6, 19.1 Ω after 0, 10, 50 cycles, respectively) and R<sub>ct</sub> (113.2, 198.8, and 302.6 Ω after 0, 10, 50 cycles, respectively). R<sub>el</sub> contains electrode and electrolyte impedances. The increase in R<sub>ct</sub> may be more directly attributed to the formation of SEI, since it is insulating and slows down the electrode reaction process.<sup>[46]</sup> The smaller R<sub>ct</sub> and R<sub>el</sub> indicate that the CNF/Se cell with the C-coated separator is much more stable during long-term cycling and involves less SEI content.<sup>[37]</sup> More interestingly, as evidenced in Figure 4c, 4d and Table S1, this work presents the highest Se loading (72.1 wt. %, 4.4 mg cm<sup>-2</sup>) and areal capacity (2.63 mA h cm<sup>-2</sup> obtained by multiplying the reversible specific capacity and Se loading), compared to the various reported Na-Se technologies.

Similar to the Na-S batteries, the Na-Se batteries may also suffer from self-discharge that occurs due to polyselenide shuttling during long cell rest time. Therefore, the effect of the carbon-coated separator in alleviating the cell instability requires careful investigation. As

shown in Figure 5a, the cells employing the carbon-coated separator maintain 578, 572, 571, 567, 566, 561 mA h g<sup>-1</sup> after resting, respectively, for 1, 2, 3, 4, 5, 6 months, corresponding to a static capacity fade of around 0.12%, 0.076%, 0.052%, 0.045%, 0.038%, and 0.036% per day, implying excellent suppression of the self-discharge behavior.<sup>[42]</sup> The electrochemical performances of CNF/Se with the carbon-coated separator after resting for one month are given in Figure S9b, S9c, and S9d. It is noteworthy that the cells utilizing the carbon-coated glass fiber separator exhibit superior capacities of 578, 530, 500, 482, 415, 355 mA h g<sup>-1</sup>, respectively, at the rates of 0.1, 0.2, 0.5, 2, 5C and 504 mA h g<sup>-1</sup> after 100 cycles at 0.1C rate. In comparison, cells with the pure glass fiber separator could not prevent static polyselenide shuttling as the initial charge capacity reduces from 598 to 340 mA h g<sup>-1</sup> after resting for six months.

To reveal the origin of the shuttle mechanism of the CNF/Se electrode and the effect of the carbon coating on the separator, visualized experiments and density functional theory (DFT) simulations were carried out systematically. As shown in Figure 5b and S10, the color of the electrolyte turns into red with the CNF/Se electrodes cycled 10, 50, 80, 120 times and some cycled aggregates are clearly observed on the surface of CNF after 200 cycles, as evidenced further in Figure S11b and S11c. The red product can be associated with the long-chain Se<sub>n</sub> as confirmed by the Raman spectrum shown in Figure S11d. However, as evidenced in Figure S11a, no obvious color change on the other side of glass fiber can be detected when employing the carbon-coated separator, which can be largely due to the light-weight carbon coating effectively absorbing the soluble polyselenide, as shown in Figure 5c. In addition, the robust carbon coating still keeps its structure after 200 cycles and the adsorption of polyselenide indeed occurs as demonstrated by the overall morphology (Figure 5d) and uniform elemental mapping (Figure 5e, 5f and 5g).

Based on these phenomena, molecular dynamics simulations were first performed to understand the interaction process between Se and Na, as indicated in Figure S12. It is

noteworthy that the Na atoms prefer to bind to the surface not to bulk selenium atoms, forming an interconnected network via the diffusion process, which may be associated with the poor electrochemical performance of bulk Se. Then, first-principle calculations were carried out to reveal the most stable  $\text{Na}_2\text{Se}_n$  cluster structure and its combination with graphite substrate together with ethylene carbonate/dimethyl carbonate electrolyte (EC/DMC) by selecting two representative compounds ( $\text{Na}_2\text{Se}_6$  and  $\text{Na}_2\text{Se}$ ). The C=O bond would not be broken during the combination process between  $\text{Na}_2\text{Se}_x$  and EC/DMC due to the very large energy barrier and unstable EC, DMC broken pieces, as shown in Figure S13. The fully relaxed binding geometries of single  $\text{Na}_2\text{Se}_6/\text{Na}_2\text{Se}$  molecular,  $\text{Na}_4\text{Se}_{12}/\text{Na}_4\text{Se}_2$  molecule clusters,  $\text{Na}_2\text{Se}_6/\text{Na}_2\text{Se}$  with DMC/EC molecules as well as  $\text{Na}_2\text{Se}_6/\text{Na}_2\text{Se}$  on the graphite surface are demonstrated in Figure 6a-6l. According to the pore size distributions and optimized  $\text{Na}_2\text{Se}_6$ , DMC, EC,  $\text{Na}_2\text{Se}_6$ -EC,  $\text{Na}_2\text{Se}_6$ -DMC structures as shown in Figure S6 and S14, it is expected that EC/DMC would be able to penetrate between the impregnated Se and the CNF matrix. Therefore,  $\text{Na}_2\text{Se}_6$  prefers to dissolve into the electrolyte due to stronger binding energies (1.66 eV for EC, 1.78 eV for DMC) than that of  $\text{Na}_4\text{Se}_{12}$  (1.41 eV),  $\text{Na}_2\text{Se}_6$  molecular-graphite substrate (0.42 eV), and  $\text{Na}_2\text{Se}_6$  molecular-heteroatom O doped graphite substrate (1.47 eV).<sup>30</sup> On the contrary, as displayed in Figure 6e-6l, the formation energies of the  $\text{Na}_4\text{Se}_2$  clusters (2.26 eV) and the binding energies of the  $\text{Na}_2\text{Se}$  molecular-heteroatom O doped graphite substrate (2.01 eV) are much larger than that of  $\text{Na}_2\text{Se}$ -EC (1.61 eV) and  $\text{Na}_2\text{Se}$ -DMC (1.52 eV), indicating higher-order  $\text{Na}_2\text{Se}$  clusters tend to agglomerate into a solid network rather than dissolve into the electrolyte, thus shedding light on the understanding of the shuttle mechanism of the CNF/Se electrode and the effect of carbon-coating on the separator.

### 3. Conclusion

In conclusion, we have rationally designed a binder-free, self-interwoven CNF/Se electrode by infiltrating Se into KOH activated porous carbon nanofiber that has been coupled with a light-weight carbon-coated separator for Na-Se batteries through a facile fabrication process. This robust electrode structure enables high Se content (72.1 wt. %) and loading (4.4 mg cm<sup>-2</sup>) and improved dynamic (cycle life) and static (shelf-life) stabilities with highly reversible capacities of 599 mA h g<sup>-1</sup> at 0.1C rate and 382 mA h g<sup>-1</sup> at 5C rate. Additionally, an analysis of the cycled products together with DFT simulation results have demonstrated the ability of this cell configuration for suppressing sodium poly selenide migration between the cathode and anode, thus making the Na-Se cells competitive for energy storage.

### Experimental Section

Supporting Information provides the detailed synthesis methods of the selenium cathodes, RT Na-Se cells, and the structural and electrochemical measurement methods.

### Supporting Information

Supporting Information is available from the Wiley Online Library or from the author.

### Acknowledgements

This work was supported by the U.S. Department of Energy, Office of Basic Energy Sciences, Division of Materials Science and Engineering under award number DE-SC0005397. One of the authors (H. W) thanks the China Scholarship Council (Grant No. 201606690005) for the award of a fellowship.

Received: ((will be filled in by the editorial staff))

Revised: ((will be filled in by the editorial staff))

Published online: ((will be filled in by the editorial staff))

## References

- [1] Goodenough, J.B., *Energy Environ. Sci.* **2014**, *7*, 14.
- [2] Melot, B.C., J.M. Tarascon, *Accounts. Chem. Res.* **2013**, *46*, 1226.
- [3] Zhu, S., J. Li, X. Deng, C. He, E. Liu, F. He, C. Shi, N. Zhao, *Adv. Funct. Mater.* **2017**, *27*, 1605017.
- [4] Zheng, Q., Z. Niu, J. Ye, S. Zhang, L. Zhang, L. Li, Y. Zhao, X. Zhang, *Adv. Funct. Mater.* **2017**, *27*, 1604299.
- [5] He, G., X. Han, R. Zou, T. Zhao, Z. Weng, S. Ho-Kimura, Y. Lu, H. Wang, Z.X. Guo, I.P. Parkin, *Adv. Funct. Mater.* **2017**, *27*, 1604903.
- [6] Yang, C., X. Ou, X. Xiong, F. Zheng, R. Hu, Y. Chen, M. Liu, K. Huang, *Energy Environ. Sci.* **2017**, *10*, 107.
- [7] Guo, S., P. Liu, S. Yang, K. Zhu, Y. Jin, M. Chen, I. Masayoshi, H. Zhou, *Angewandte Chemie International Edition* **2015**, *54*, 11701.
- [8] Xie, F., L. Zhang, D. Su, M. Jaroniec, S.Z. Qiao, *Adv. Mater.* **2017**, *29*, 1700989.
- [9] Slater, M.D., D. Kim, E. Lee, C.S. Johnson, *Adv. Funct. Mater.* **2013**, *23*, 947.
- [10] Zhao, L., J. Zhao, Y.S. Hu, H. Li, Z. Zhou, M. Armand, L. Chen, *Adv. Energy Mater.* **2012**, *2*, 962.
- [11] Jian, Z., W. Han, X. Lu, H. Yang, Y.-S. Hu, J. Zhou, Z. Zhou, J. Li, W. Chen, D. Chen, L. Chen, *Adv. Energy Mater.* **2013**, *3*, 156.
- [12] Li, S., Y. Dong, L. Xu, X. Xu, L. He, L. Mai, *Adv. Mater.* **2014**, *26*, 3545.
- [13] Yabuuchi, N., K. Kubota, M. Dahbi, S. Komaba, *Chem. Rev.* **2014**, *114*, 11636.
- [14] Ou, X., J. Li, F. Zheng, P. Wu, Q. Pan, X. Xiong, C. Yang, M. Liu, *J. Power Sources* **2017**, *343*, 483.

[15] Ong, S.P., V.L. Chevrier, G. Hautier, A. Jain, C. Moore, S. Kim, X. Ma, G. Ceder, *Energy Environ. Sci.* **2011**, *4*, 3680.

[16] Masquelier, C., L. Croguennec, *Chem. Rev.* **2013**, *113*, 6552.

[17] Zhang, K., Z. Hu, X. Liu, Z. Tao, J. Chen, *Adv. Mater.* **2015**, *27*,

[18] Ou, X., C. Yang, X. Xiong, F. Zheng, Q. Pan, C. Jin, M. Liu, K. Huang, *Adv. Funct. Mater.* **2017**, *27*, 1606242.

[19] Dae Hoe, L., X. Jing, M. Ying Shirley, *Phys.chem.chem.phys* **2013**, *15*, 3304.

[20] Zhao, W., G. Zhong, M.J. McDonald, Z. Gong, R. Liu, J. Bai, C. Yang, S. Li, W. Zhao, H. Wang, R. Fu, Z. Jiang, Y. Yang, *Nano Energy* **2016**, *27*, 420.

[21] Wang, H., L. Wang, S. Chen, G. Li, J. Quan, E. Xu, L. Song, Y. Jiang, *J. Mater. Chem. A* **2017**, *5*, 3569.

[22] Pan, H., X. Lu, X. Yu, Y.S. Hu, H. Li, X.Q. Yang, L. Chen, *Adv. Energy Mater.* **2013**, *3*, 1186.

[23] Liu, H., D. Su, R. Zhou, B. Sun, G. Wang, S.Z. Qiao, *Adv. Energy Mater.* **2012**, *2*, 970.

[24] Chang, K., D. Geng, X. Li, J. Yang, Y. Tang, M. Cai, R. Li, X. Sun, *Adv. Energy Mater.* **2013**, *3*, 839.

[25] Carter, R.E., L. Oakes, A. Douglas, N. Muralidharan, A.P. Cohn, C.L. Pint, *Nano Lett* **2017**, *17*, 1863.

[26] Fan, L., R. Ma, Y. Yang, S. Chen, B. Lu, *Nano Energy* **2016**, *28*, 304.

[27] Xin, S., Y.X. Yin, Y.G. Guo, L.J. Wan, *Adv. Mater.* **2014**, *26*, 1261.

[28] Wen, Z., Y. Hu, X. Wu, J. Han, Z. Gu, *Adv. Funct. Mater.* **2013**, *23*, 1005.

[29] Zheng, S., P. Han, Z. Han, P. Li, H. Zhang, J. Yang, *Adv. Energy Mater.* **2014**, *4*, 1400226.

[30] Yu, X., A. Manthiram, *Adv. Energy Mater.* **2015**, *5*, 1500350.

[31] Wang, Y.-X., J. Yang, W. Lai, S.-L. Chou, Q.-F. Gu, H.K. Liu, D. Zhao, S.X. Dou, *J. Am. Chem. Soc.* **2016**, *138*, 16576.

[32] Liu, Y., Z. Tai, Q. Zhang, H. Wang, W.K. Pang, H.K. Liu, K. Konstantinov, Z. Guo, *Nano Energy* **2017**, *35*, 36.

[33] Li, Z., L. Yuan, Z. Yi, Y. Liu, Y. Huang, *Nano Energy* **2014**, *9*, 229.

[34] Xin, S., L. Yu, Y. You, H.-P. Cong, Y.-X. Yin, X.-L. Du, Y.-G. Guo, S.-H. Yu, Y. Cui, J.B. Goodenough, *Nano Lett* **2016**, *16*, 4560.

[35] Abouimrane, A., D. Dambournet, K.W. Chapman, P.J. Chupas, W. Weng, K. Amine, *J. Am. Chem. Soc.* **2012**, *134*, 4505.

[36] Yang, C.-P., Y.-X. Yin, Y.-G. Guo, *The Journal of Physical Chemistry Letters* **2015**, *6*, 256.

[37] Ding, J., H. Zhou, H. Zhang, T. Stephenson, Z. Li, D. Karpuzov, D. Mitlin, *Energy Environ. Sci.* **2017**, *10*, 153.

[38] Li, X., J. Liang, Z. Hou, W. Zhang, Y. Wang, Y. Zhu, Y. Qian, *Adv. Funct. Mater.* **2015**, *25*, 5229.

[39] Luo, C., Y. Xu, Y. Zhu, Y. Liu, S. Zheng, Y. Liu, A. Langrock, C. Wang, *Acs Nano* **2013**, *7*, 8003.

[40] Wang, H., S. Li, Z. Chen, H.K. Liu, Z. Guo, *RSC Advances* **2014**, *4*, 61673.

[41] Zeng, L., W. Zeng, Y. Jiang, X. Wei, W. Li, C. Yang, Y. Zhu, Y. Yu, *Adv. Energy Mater.* **2014**, *5*, 1401377.

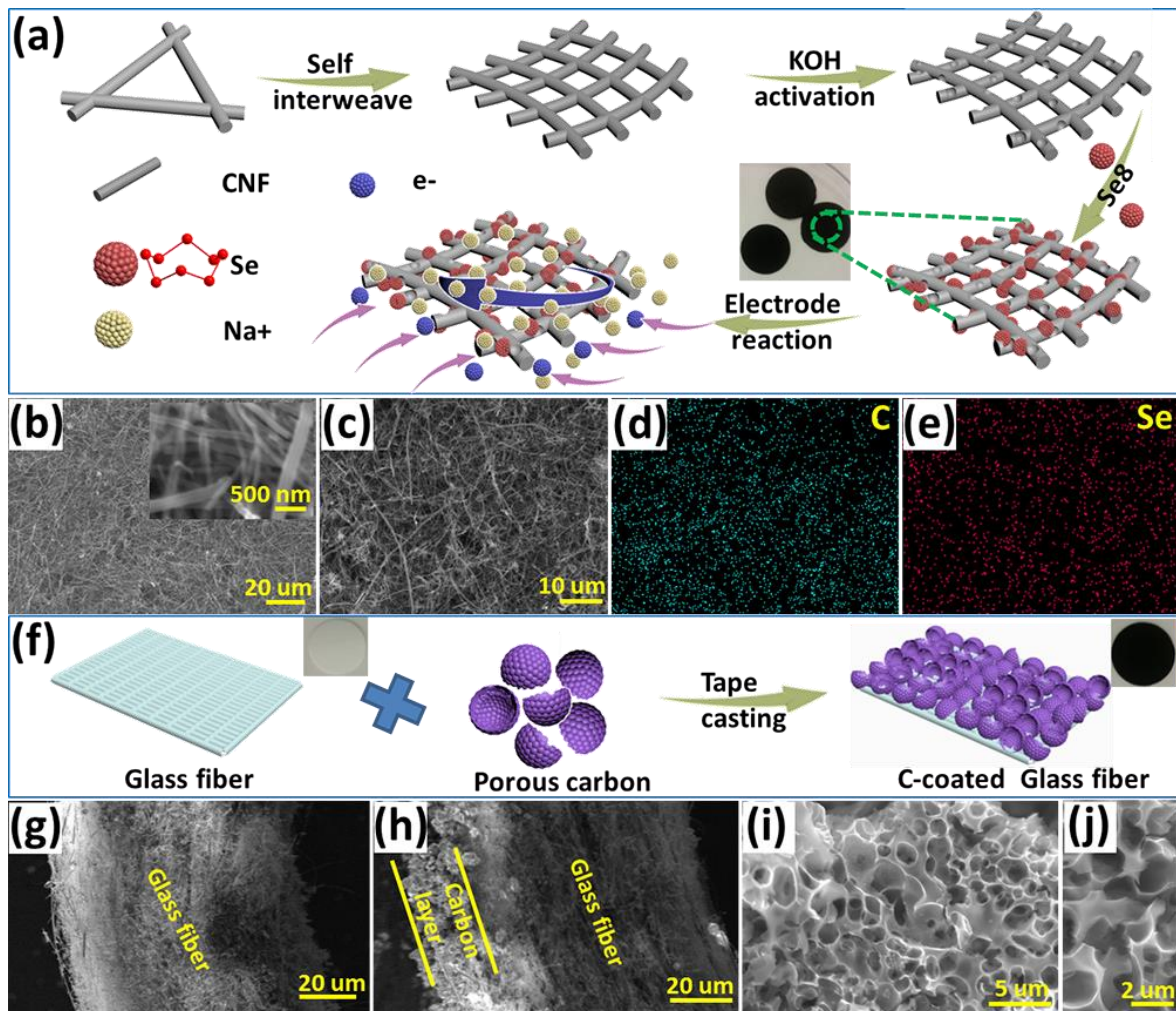
[42] Chung, S.-H., A. Manthiram, *Adv. Funct. Mater.* **2014**, *24*, 5299.

[43] Li, Q., H. Liu, Z. Yao, J. Cheng, T. Li, Y. Li, C. Wolverton, J. Wu, V.P. Dravid, *Acs Nano* **2016**, *10*, 8788.

[44] Memarzadeh Lotfabad, E., P. Kalisvaart, A. Kohandehghan, D. Karpuzov, D. Mitlin, *J. Mater. Chem. A* **2014**, *2*, 19685.

[45] Zu, C., A. Manthiram, *Adv. Energy Mater.* **2013**, *3*, 1008.

[46] Ji, L., M. Gu, Y. Shao, X. Li, M.H. Engelhard, B.W. Arey, W. Wang, Z. Nie, J. Xiao, C. Wang, *Adv. Mater.* **2014**, *26*, 2901.

**Figures**

**Figure 1.** (a, f) Schematic illustration of the synthesis process of the CNF/Se electrode and light-weight carbon-coated separator. (b, c) FESEM images of the fabricated CNF/Se composite electrode. (d, e) Elemental mapping images of the CNF/Se composite electrode. (g, h, i, j) FESEM images of the glass fiber and carbon-coated glass fiber cross sections and surface of the light-weight carbon coating.

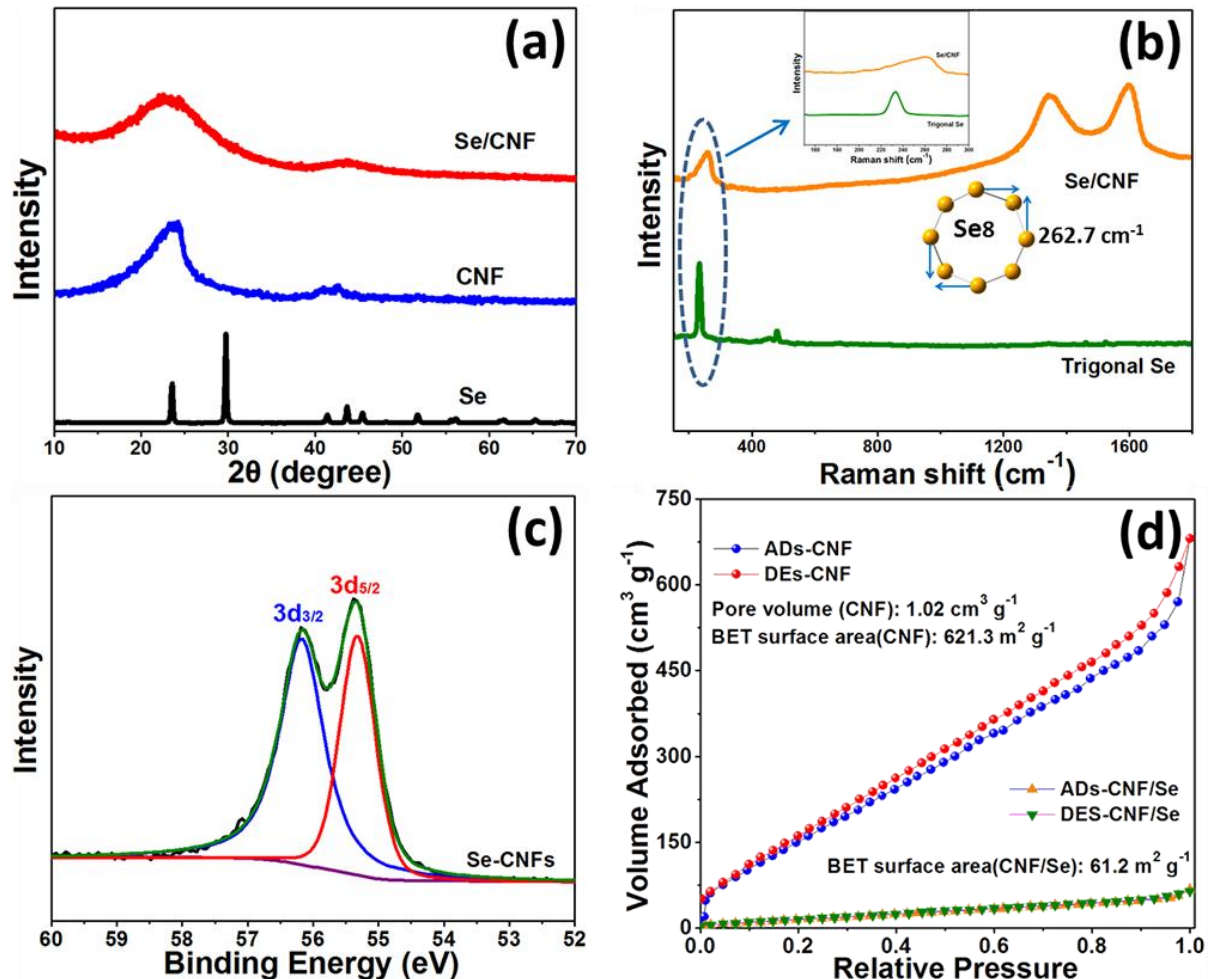


**Figure 2.** (a) XRD patterns of bulk Se, CNF, and CNF/Se composite. (b) Raman spectra of bulk Se and CNF/Se. (c) High-resolution XPS spectrum of Se 3d for CNF/Se. (d) Nitrogen adsorption–desorption isotherms of KOH activated CNF and CNF/Se composite.

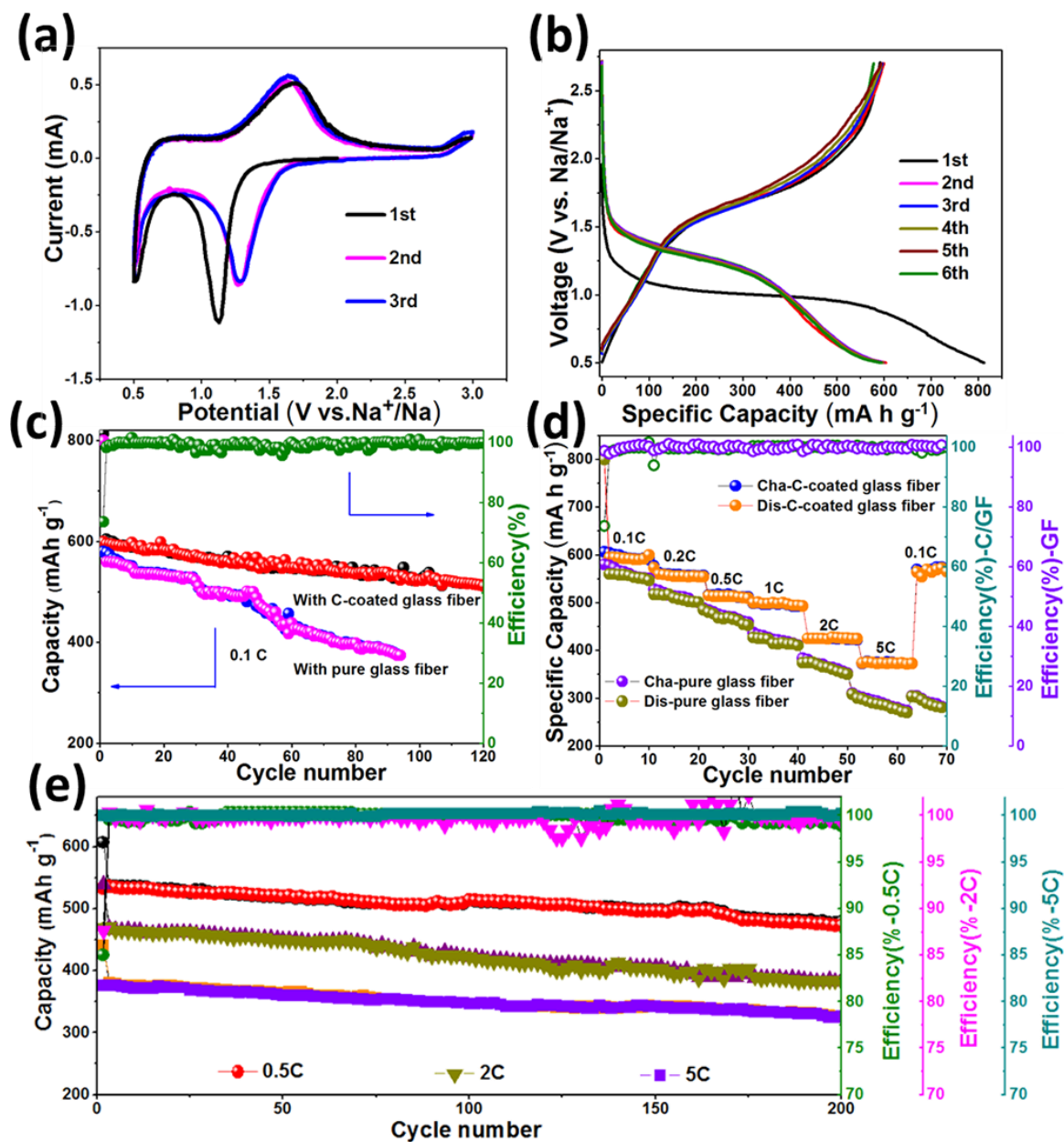


**Figure 3.** Electrochemical measurements of Na-Se cells. (a) Cyclic voltammograms of the cell with a light-weight carbon-coated separator. (b) Discharge-charge curves of the cells with a light-weight carbon-coated separator. (c) Cycling performance of the Na-Se cells with a light-weight carbon-coated and pure glass fiber separator. (d) Discharge-charge capacities of cells utilizing a light-weight carbon-coated and pure glass fiber separator at various cycling rates. (e) Long-term cycle life of the cells with a light-weight carbon-coated separator at 0.5C, 2C and 5C rates.

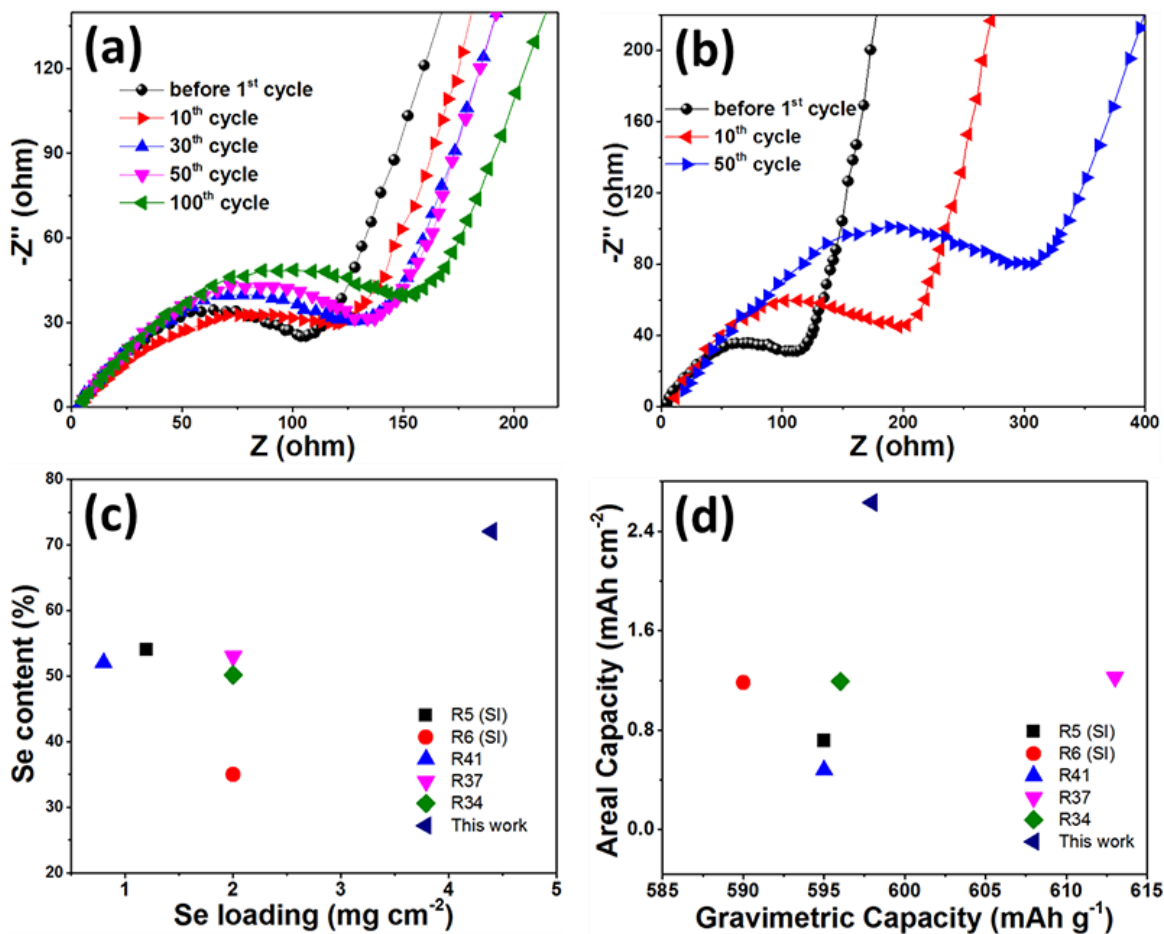


**Figure 4.** (a, b) Cell impedance tests of the CNF/Se electrode with a light-weight carbon-coated separator and pure glass fiber separator. (c) Comparison of the Se content and loading from the literature and this work. (d) Comparison of the areal capacities from the literature and this work.

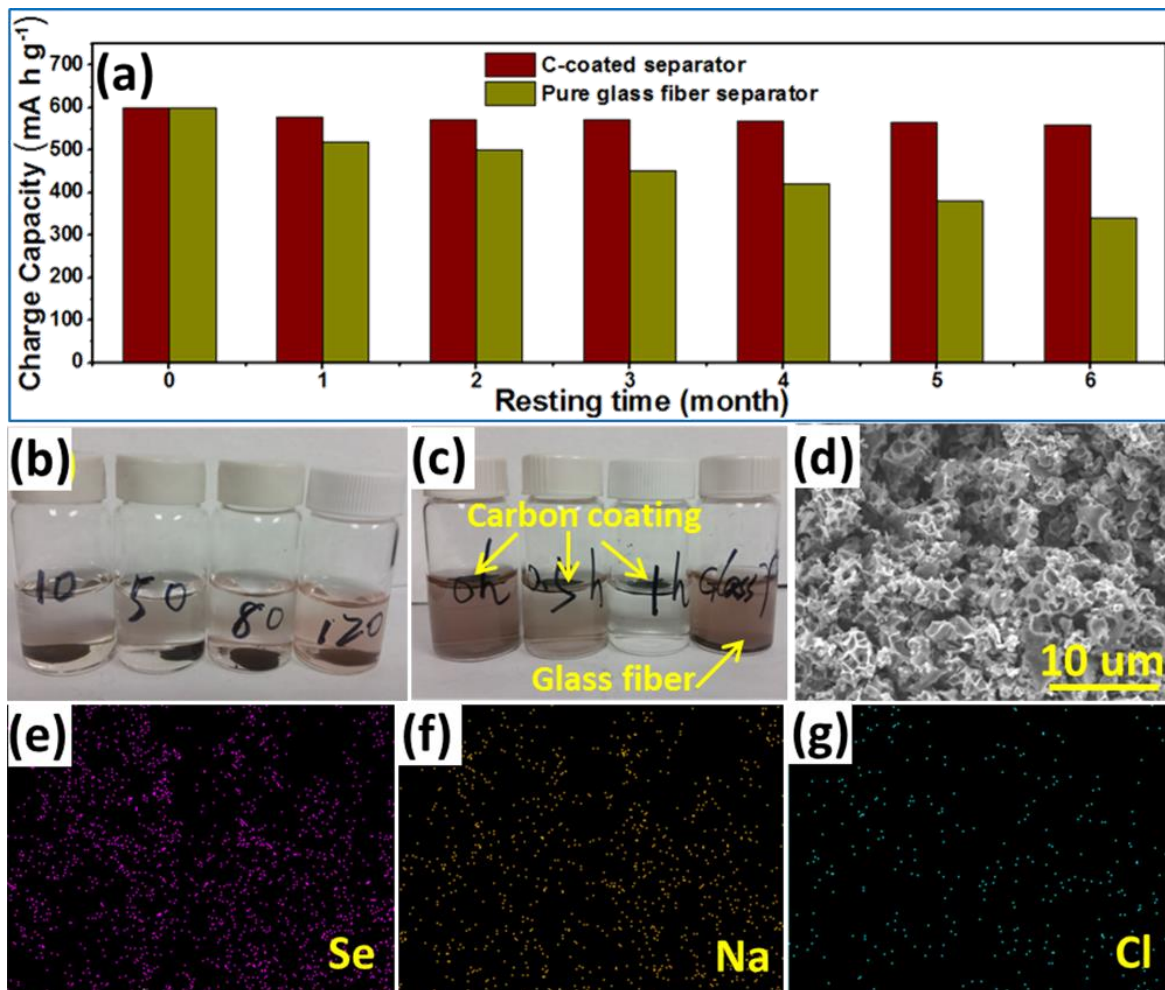


**Figure 5.** Static electrochemical stability: (a) Charge capacity retention of the cells after storing for various times. (b) Photographs of the CNFs/Se (prepared at 260 °C) electrodes in the electrolyte after cycling for 10, 50, 80, 120 cycles; the numbers on the bottles refer to number of cycles. (c) Comparison of the photographs of the carbon coating (stripped from a separator) in a polyselenide solution after 0, 0.5, 1 h with that of pure glass fiber in a polyselenide solution after 12 h. (d) FESEM images, and (e, f, g) elemental mapping of the carbon-coated surface after 200 cycles (discharged to 0.5 V).

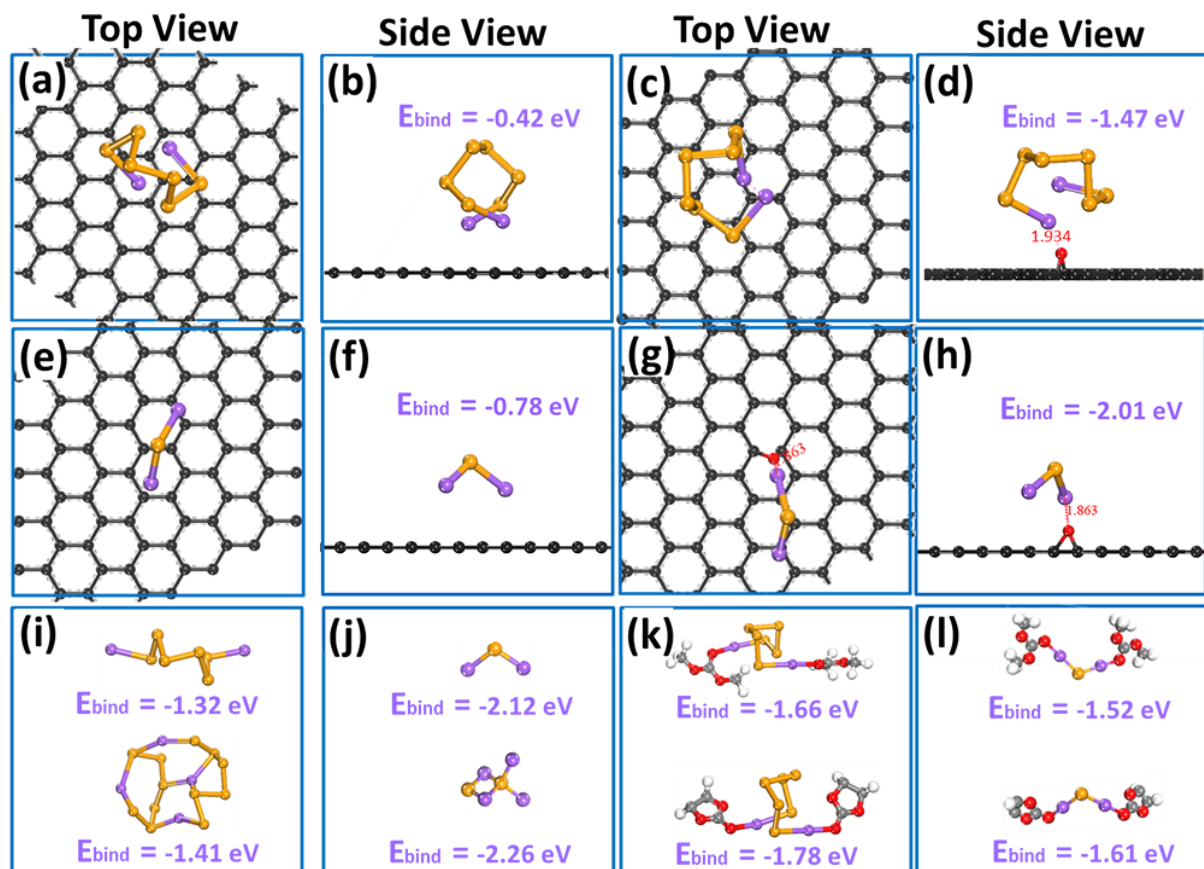


**Figure 6.** (a, b, c, d) Binding energies of  $\text{Na}_2\text{Se}_6$  with pristine graphite substrates and O-doped graphite substrates. (e, f, g, h) Binding energies of  $\text{Na}_2\text{Se}$  with pristine graphite substrates and O-doped graphite substrates. (i, j) Calculated binding energies of the most stable  $\text{Na}_2\text{Se}_6/\text{Na}_4\text{Se}_{12}$  cluster, and  $\text{Na}_2\text{Se}/\text{Na}_4\text{Se}_2$  cluster. (k, l) Binding energies of the  $\text{Na}_2\text{Se}_6$  cluster and  $\text{Na}_2\text{Se}$  with DMC and EC. Gray, white, brown, purple, and red balls represent carbon, hydrogen, selenium, sodium and oxygen atoms, respectively.

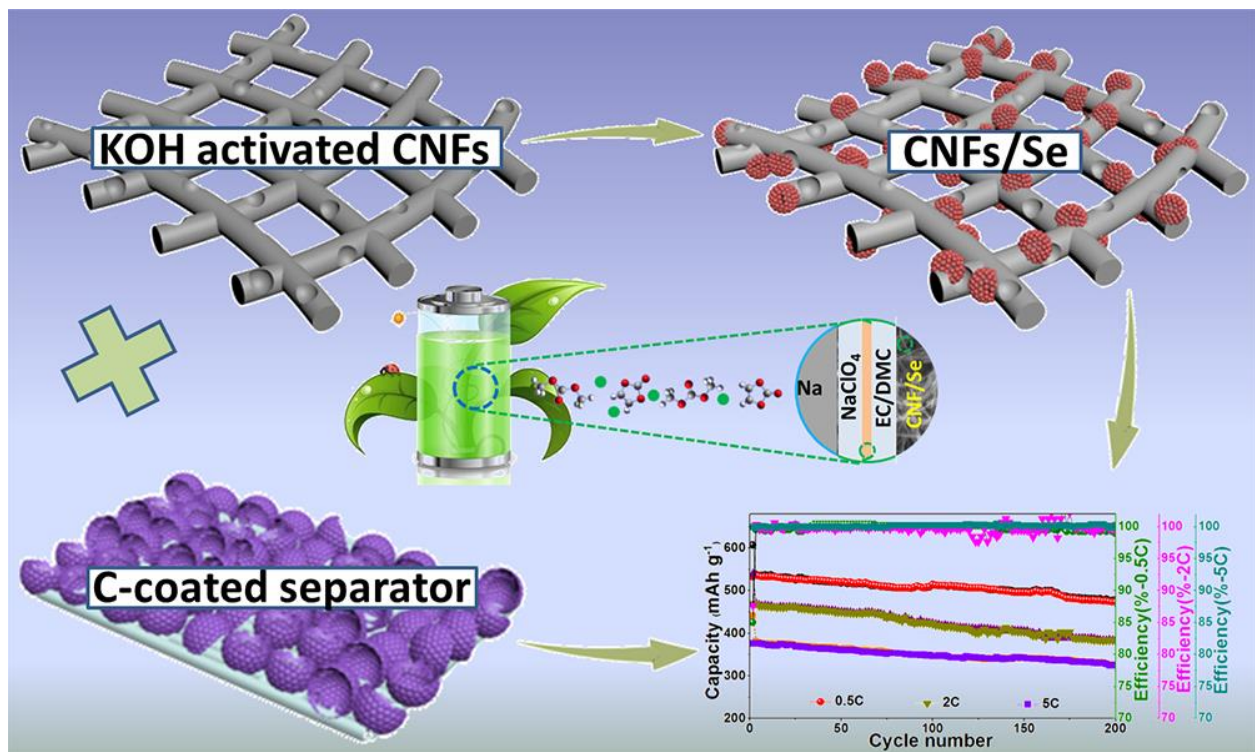
## Table of Contents

**A novel Na-Se cell**, assembled by coupling self-interwoven CNF/Se with a carbon-coated separator displays excellent cycling life stability with a high selenium loading of  $4.4 \text{ mg cm}^{-2}$ . The cell also retains 93.4% of its initial capacity even after resting for six months, making the Na-Se cells competitive for energy storage.

**Keywords:** sodium-selenium batteries, carbon nanofiber-selenium cathode, high selenium loading, carbon-coated separator, polyselenide shuttle

**Long cycle life, low self-discharge sodium-selenium batteries with high selenium loading and suppressed polyselenide shuttling**

*Hui Wang,<sup>a,b</sup> Yang Jiang,<sup>b,\*</sup> and Arumugam Manthiram<sup>a,\*</sup>*



Copyright WILEY-VCH Verlag GmbH & Co. KGaA, 69469 Weinheim, Germany, 2017.

# ADVANCED ENERGY MATERIALS

## Supporting Information

### Long cycle life, low self-discharge sodium-selenium batteries with high selenium loading and suppressed polyselenide shuttling

*Hui Wang,<sup>a,b</sup> Yang Jiang,<sup>b,\*</sup> and Arumugam Manthiram<sup>a,\*</sup>*

Dr. Hui Wang, Prof. A. Manthiram

<sup>a</sup> Materials Science and Engineering Program & Texas Materials Institute, The University of Texas at Austin, Austin , TX 78712 , USA

E-mail: [manth@austin.utexas.edu](mailto:manth@austin.utexas.edu)

Dr. Hui Wang, Prof. Yang Jiang

<sup>b</sup> School of Materials Science and Engineering, Hefei University of Technology, Hefei, Anhui 230009, P. R. China.

E-mail: [apjiang@hfut.edu.cn](mailto:apjiang@hfut.edu.cn).

## Experimental Section

*Preparation of KOH activated CNF Paper:* First, the carbon nanofiber (CNF) paper was prepared through a facile vacuum filtration and peel-off method.<sup>[1]</sup> Typically, CNF (200 mg, Pyrograf Products, Inc.) was dispersed in 100 ml isopropyl alcohol under ultrasonication condition. Then, the suspension was directly vacuum filtered and the CNF paper was peeled off from the filter membrane and dried at 80 °C for 24 h. After that, the CNF papers were immersed in 1 M KOH solution for 20 h and dried at 100 °C for 24 h. Finally, the porous CNF

paper was heated under the protection of argon atmosphere with a heating rate of  $10\text{ }^{\circ}\text{C min}^{-1}$  to  $750\text{ }^{\circ}\text{C}$  and held there for 2.5 h to acquire the porous CNF paper.

*Preparation of CNF-Selenium cathode:* The obtained CNF papers were cut into circular sheets with diameters of 1 cm and a weight of around 1.2 mg according to Figure S2. Next, the mixture of CNF sheets and bulk Se (weight ratio of 1:3) was co-heated at a rate of  $2\text{ }^{\circ}\text{C min}^{-1}$  from room temperature to  $260\text{ }^{\circ}\text{C}$  and held there for 24 h at  $260\text{ }^{\circ}\text{C}$  under argon atmosphere to get the CNF/Se electrode. The calculated mass loading of Se is around  $4.4\text{ mg cm}^{-2}$  as shown in Figure S2 ( $4.4\text{ mg cm}^{-2} = (4.65 - 1.20\text{ mg}) / 0.78\text{ cm}^2$ ).

*Preparation of ultralight-weight carbon-coated separator:* First, the carbon slurry was obtained by mixing the KOH-activated carbon black with isopropyl alcohol for 24 h. Then, the C-coated glass fiber separator was prepared through a facile tape casting method. Next, it was dried for 24 h at  $60\text{ }^{\circ}\text{C}$  in a vacuum oven. Finally, the carbon-coated separator was cut into circular plates with the weight of the carbon coating around  $0.85\text{ mg (0.3 mg cm}^{-2}\text{)}$  based on Figure S2.

*Materials Characterization:* The morphologies of the CNF/Se and carbon-coated separator were examined with a FEI Quanta 650 scanning electron microscope, and the crystal structure of the CNF/Se was studied with a Philips X-ray Diffractometer (XRD) between  $10$  and  $70\text{ }^{\circ}$  at a scan rate of  $0.02\text{ }^{\circ}\text{ s}^{-1}$ . X-ray photoelectron spectroscopy (XPS, Kratos Analytical Company) was used to reveal the surface and bonding characteristics of CNF/Se. Thermogravimetric analysis (TGA) was performed (TGA 7 (Perkin-Elmer) thermogravimetric analyzer) at a scan rate of  $5\text{ }^{\circ}\text{C min}^{-1}$  from  $25\text{ }^{\circ}\text{C}$  to  $800\text{ }^{\circ}\text{C}$  under the protection of  $\text{N}_2$ . Nitrogen adsorption and desorption isotherms were carried out at  $77\text{ K}$  with an AutoSorbiQ2 (Quantachrome Instruments). The specific surface area was investigated with the BET method and density functional theory (DFT) was applied to illustrate the pore size distributions.

*Electrochemical Measurements:* The self-interwoven CNF/Se composite working electrode was evaluated with CR2032-type coin cells with Na metal as counter and either carbon-coated

or pure glass fiber as the separator. 1 M NaClO<sub>4</sub> in ethylene carbonate-dimethyl carbonate (EC: DMC = 1:1 in volume) was used as the electrolyte. Galvanostatic cycling was tested with an Arbin battery cycler at 0.5 – 2.7 V (vs. Na/Na<sup>+</sup>). The CV data were obtained with a VoltaLab PGZ 402 Potentiostat at a scan rate of 0.5 mV s<sup>-1</sup> in the voltage range of 0.5 – 3.0 V. Solartron Impedance Analyzer (Solartron 1260 A) was utilized to obtain the EIS data on the pristine and cycled CNF/Se electrodes in the frequency range of 0.1 to 1 M Hz. For *ex-situ* XRD and Raman tests, the cycled CNFs/Se electrodes were disassembled inside the glove box and then washed with EC/DMC several times. Finally, the CNF/Se electrodes were sealed in argon-filled devices for further tests.

*Computational Methods:* The calculations were conducted using density functional theory with the projector-augmented wave method.<sup>[2]</sup> Exchange-correlation functional of Perdew, Burke, and Enzerhof (PBE) was employed to analyze the exchange and correlation potential in all calculations.<sup>[3]</sup> The cut-off energy of 700 eV was used for the plane wave basis to ensure convergence. The semi-empirical London dispersion corrections of Grimme et al<sup>[4]</sup> were conducted to take the dispersion interactions of van der Waals into consideration. Single layer graphite containing heteroatom O with a 7 × 7 supercell size was introduced to understand the interaction between carbon matrix and Na<sub>2</sub>Se<sub>n</sub>. The single k point at  $\Gamma$  was adopted for all the calculation processes. The convergence error of the total energy was approximately 10<sup>-5</sup> eV/atom. The binding energy E<sub>bind</sub> of Na<sub>2</sub>Se<sub>n</sub>-EC/DMC and Na<sub>2</sub>Se<sub>n</sub>-carbon matrix is defined as  $E_{bind} = (E_{Na_2Se_n-EC/DMC/C} - E_{Na_2Se_n} - E_{EC/DMC/C})$ . The smaller negative value indicates greater binding ability. The molecular dynamics simulations were performed at room temperature for 100 ps. A time step of 1 fs was used, and the temperature was controlled by nose method.

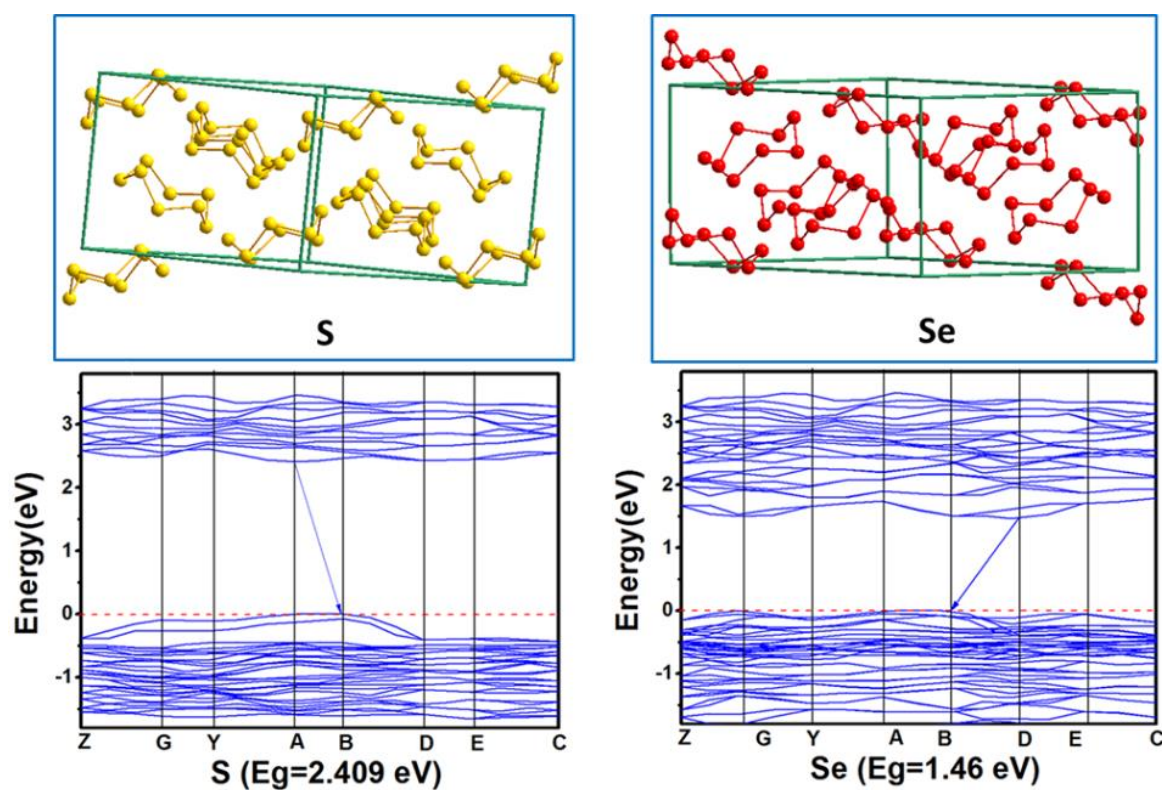


**Figure S1.** Crystal and band structures of bulk sulfur and selenium.

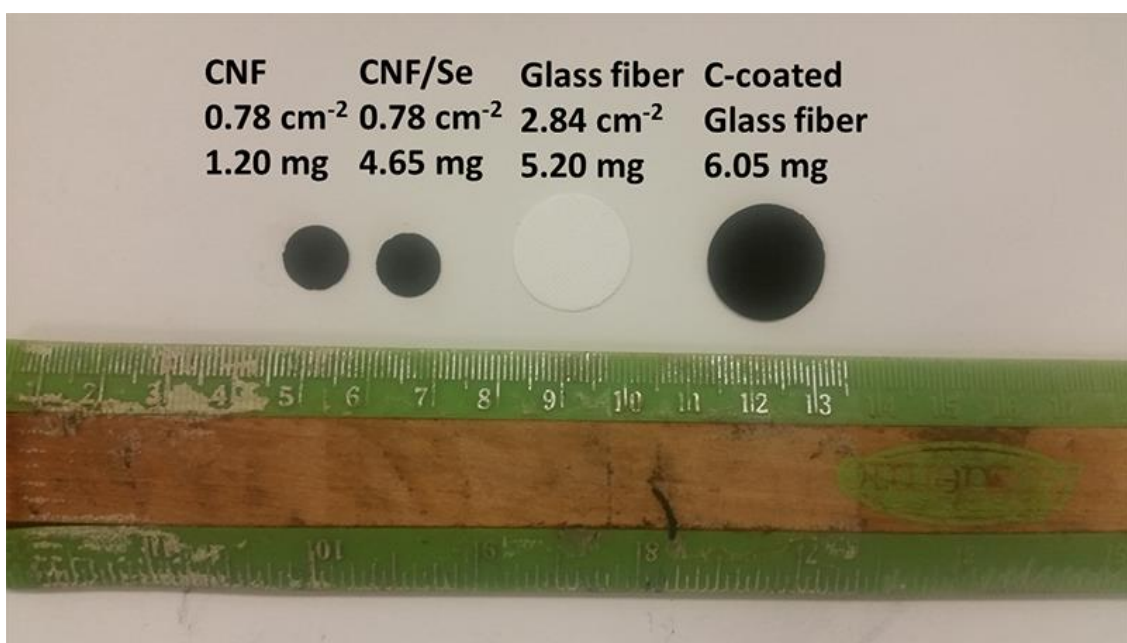


**Figure S2.** Area and weights of the CNF, CNF/Se electrode, pure glass fiber and carbon-coated glass fiber.

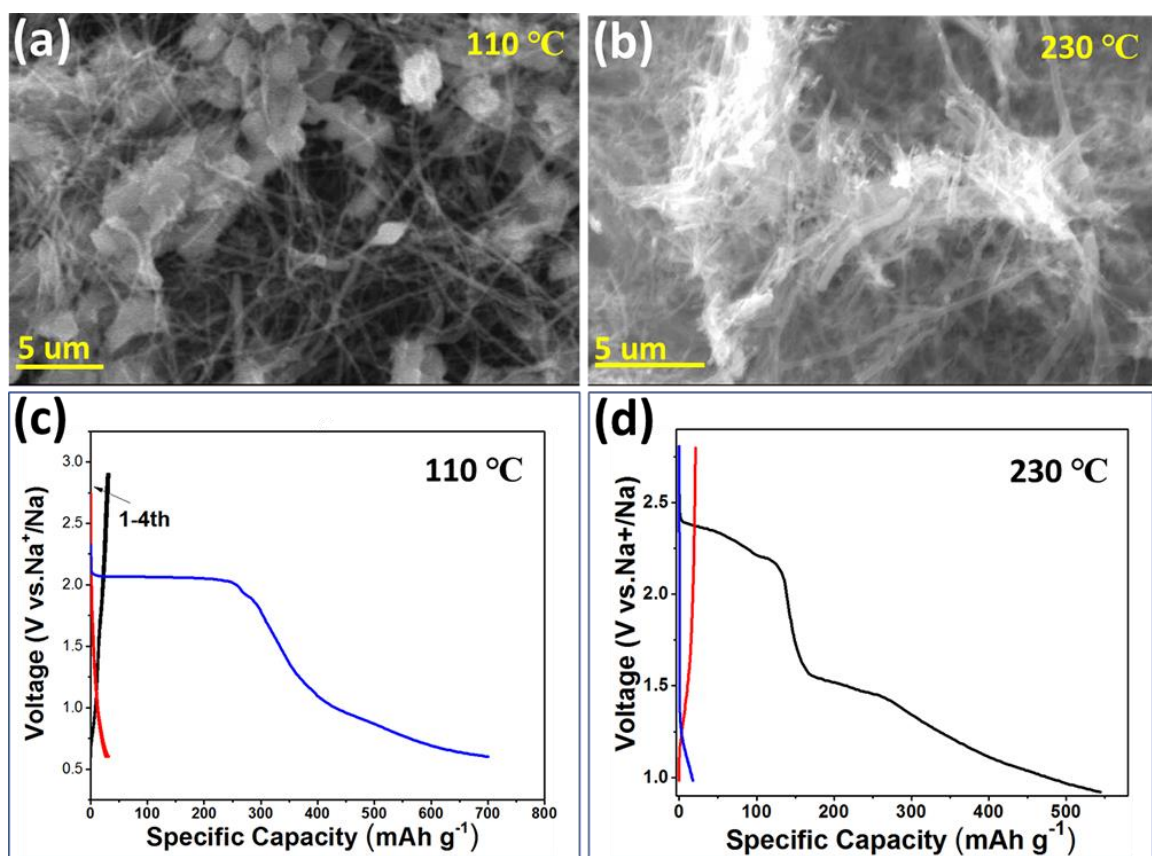


**Figure S3.** (a, b) FESEM images of the CNF/Se composite synthesized at 110 °C and 230 °C (c, d) Discharge-charge voltage profiles of CNF/Se at 110 °C and 230 °C.

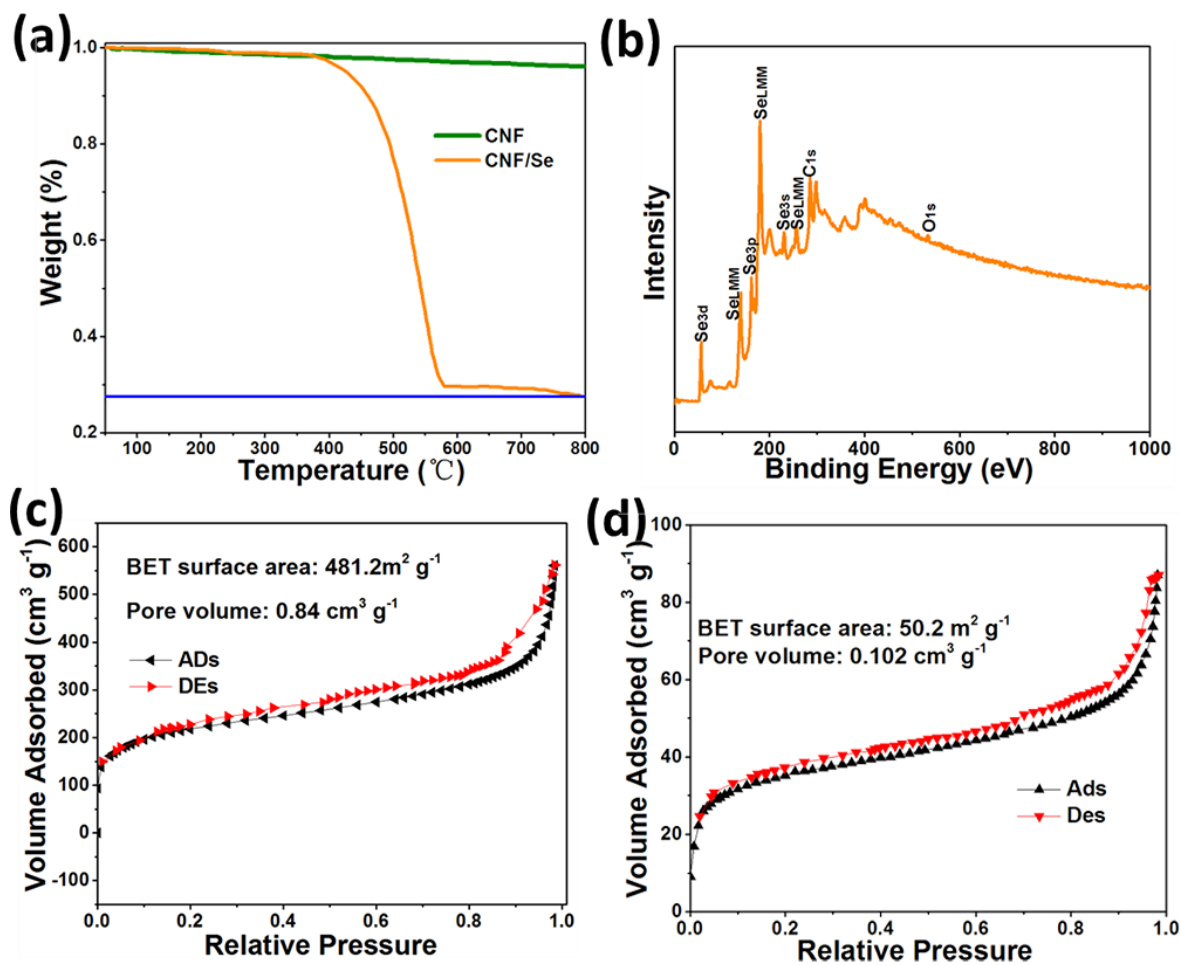


**Figure S4.** (a) Thermogravimetric (TG) plots of CNF/Se. (b) XPS spectrum of CNF/Se. (c, d) Nitrogen adsorption–desorption isotherms of ultra-light carbon and pristine CNF.

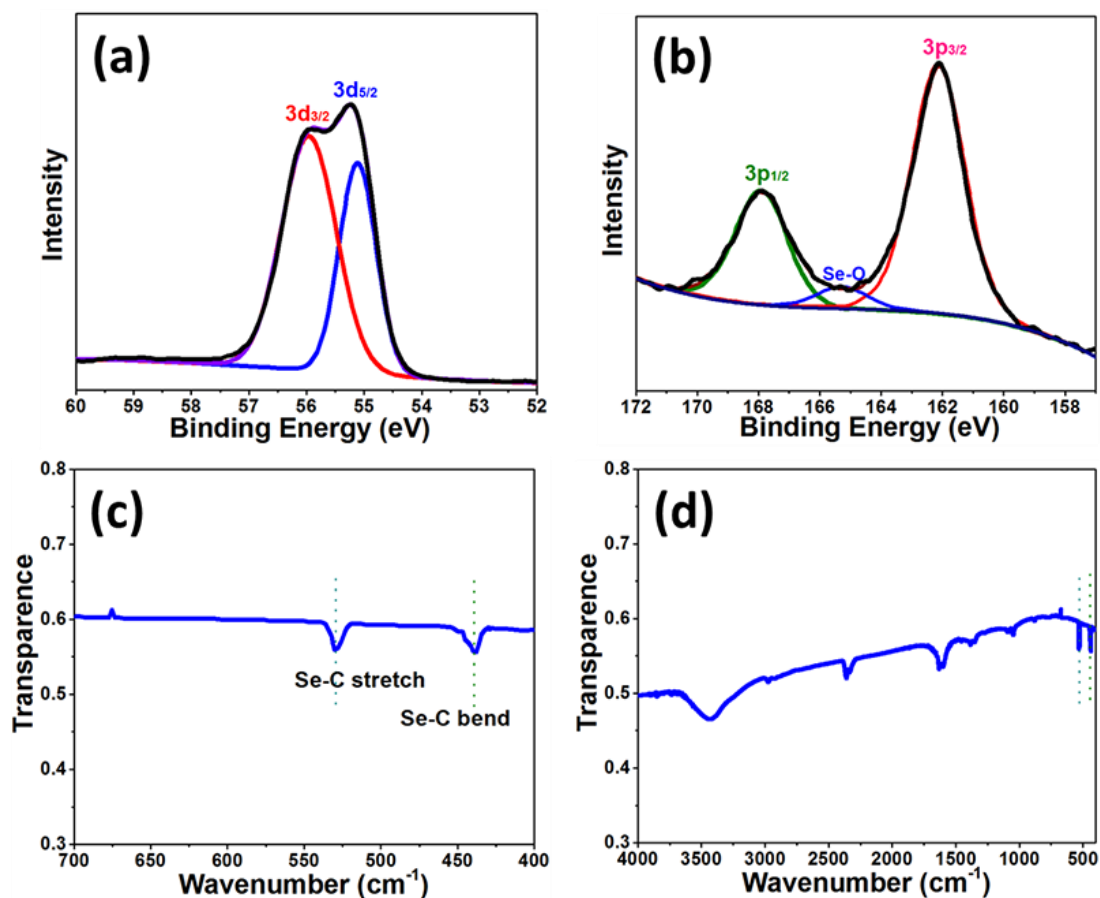


**Figure S5.** (a) High resolution XPS spectrum of Se 3d for common Se/C. (b) XPS spectrum of Se 3p for CNF/Se. (c, d) FT-IR spectrum of CNF/Se.

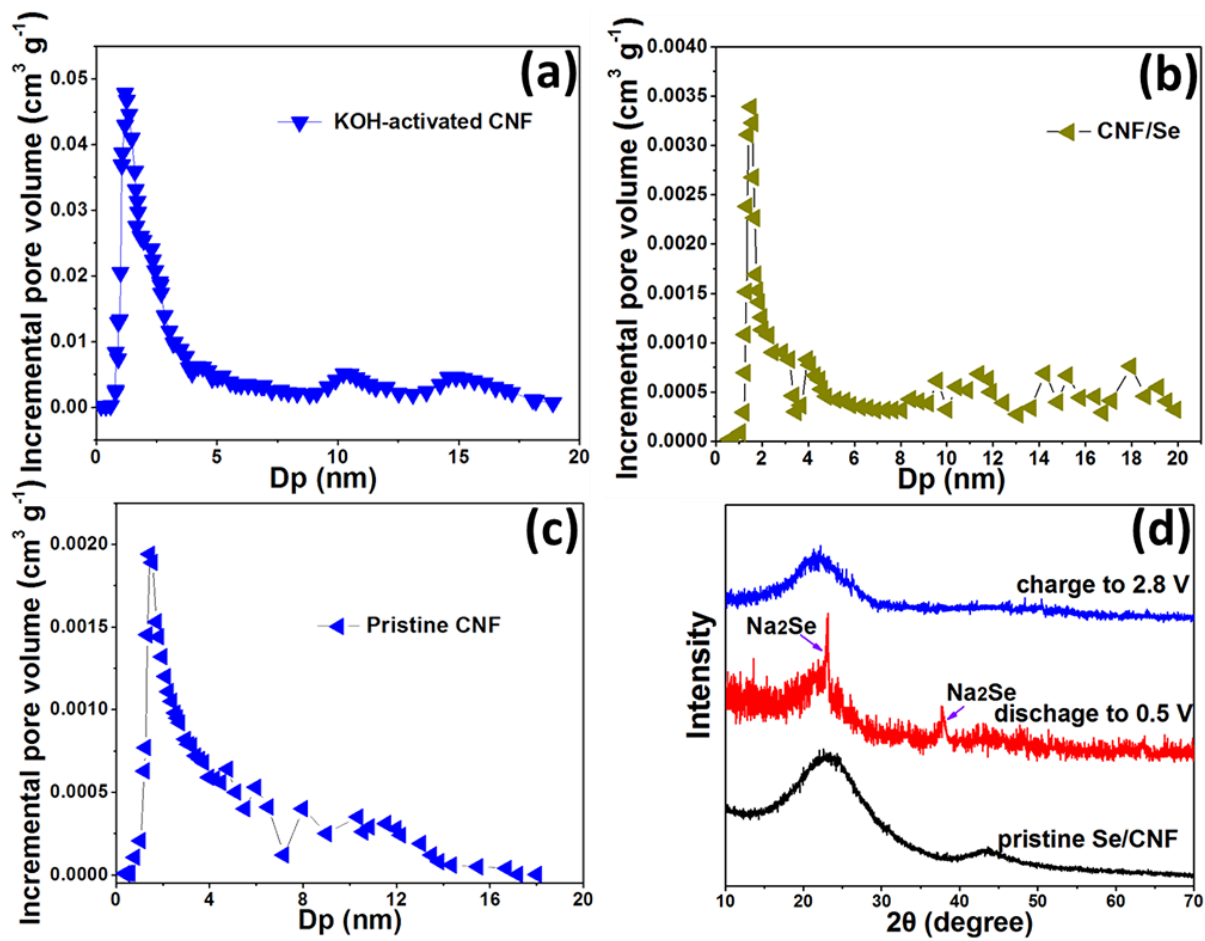


**Figure S6.** (a, b, c) Pore size distribution profiles of KOH-activated CNF and CNF/Se and pristine CNF. (d) *Ex-situ* XRD pattern of the cycled CNF/Se electrode.

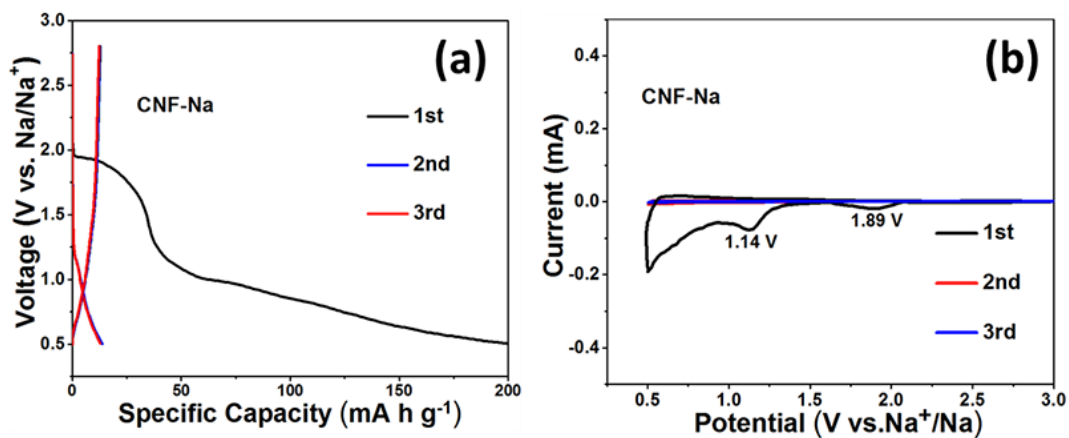
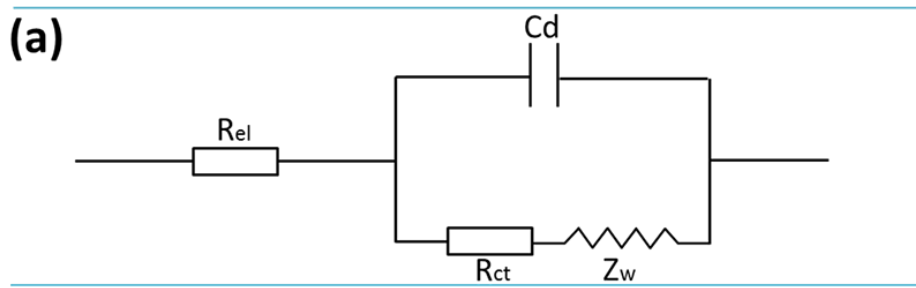


**Figure S7.** (a) Discharge-charge voltage profiles of pure CNF for the first 3 cycles for sodium storage. (b) Cyclic voltammograms of the cell with pure CNF for the first 3 cycles.



(b)

CNF/Se with C-coated separator	Before test	After 10 cycles	After 30 cycles	After 50 cycles	After 100 cycles
Rel ( $\Omega$ )	3.85	5.01	5.56	5.58	5.65
Rct ( $\Omega$ )	104.5	119.2	131.4	136.2	152.8

(c)

CNF/Se with pure glass fiber	Before test	After 10 cycles	After 50 cycles
Rel ( $\Omega$ )	5	11.6	19.1
Rct ( $\Omega$ )	113.2	198.8	302.6

**Figure S8.** (a) Equivalent circuit model of the studied system. (b, c) Resistance values were obtained by modeling the experimental impedance.

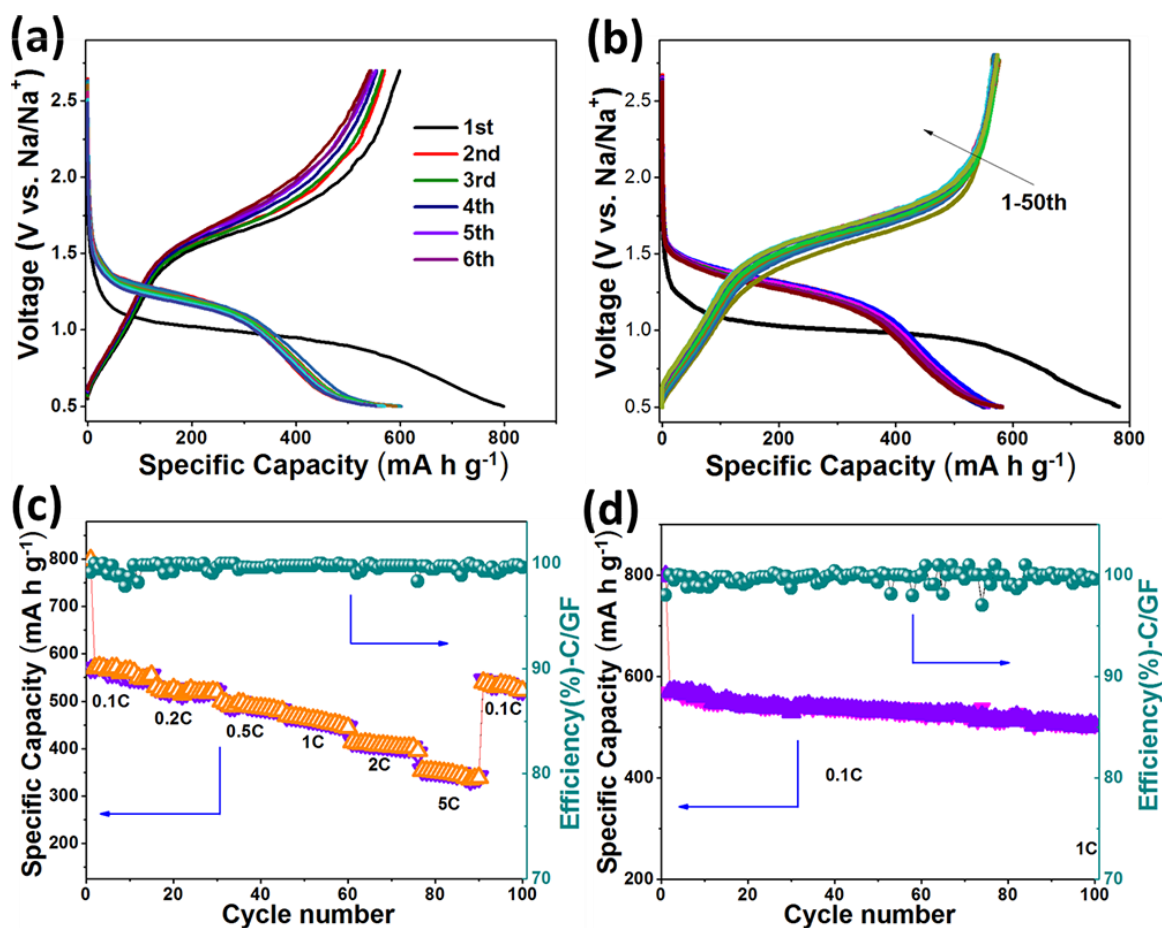


**Figure S9.** (a) Discharge-charge voltage profiles of CNF/Se with pure glass fiber separator. (b) Discharge-charge voltage profiles of CNF/Se with carbon-coated separator after resting for one month. (c, d) Rate and long cycling performance of CNF/Se with carbon-coated separator after resting for one month.

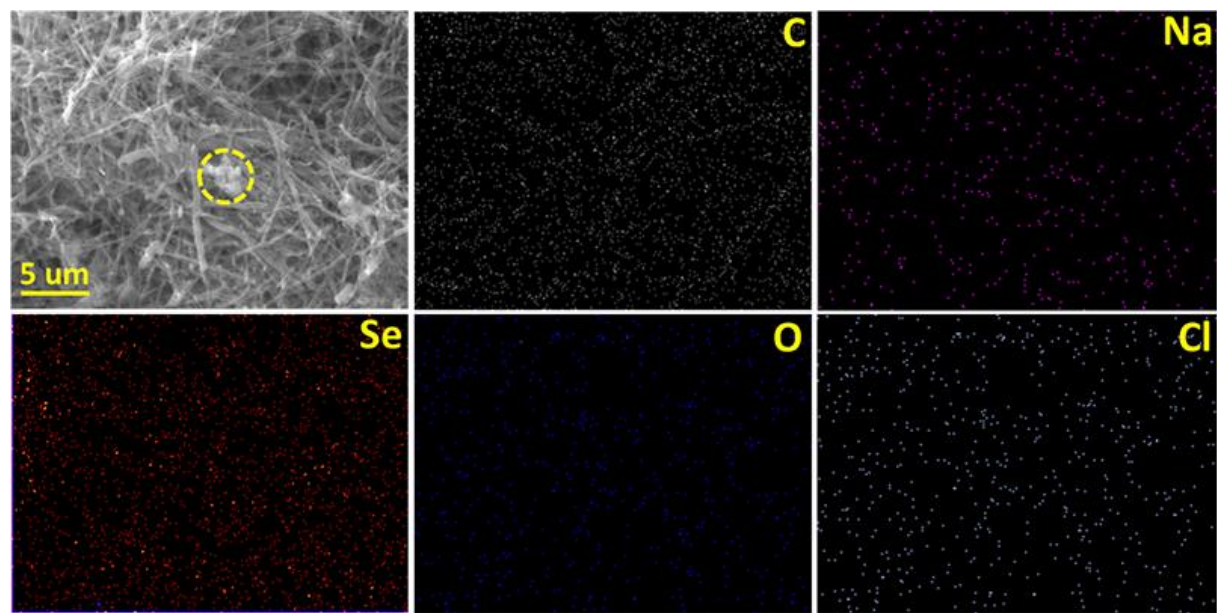


**Figure S10.** FESEM images of the CNF/Se electrode discharged to 0.5 V after 200 cycles and the corresponding mapping images.

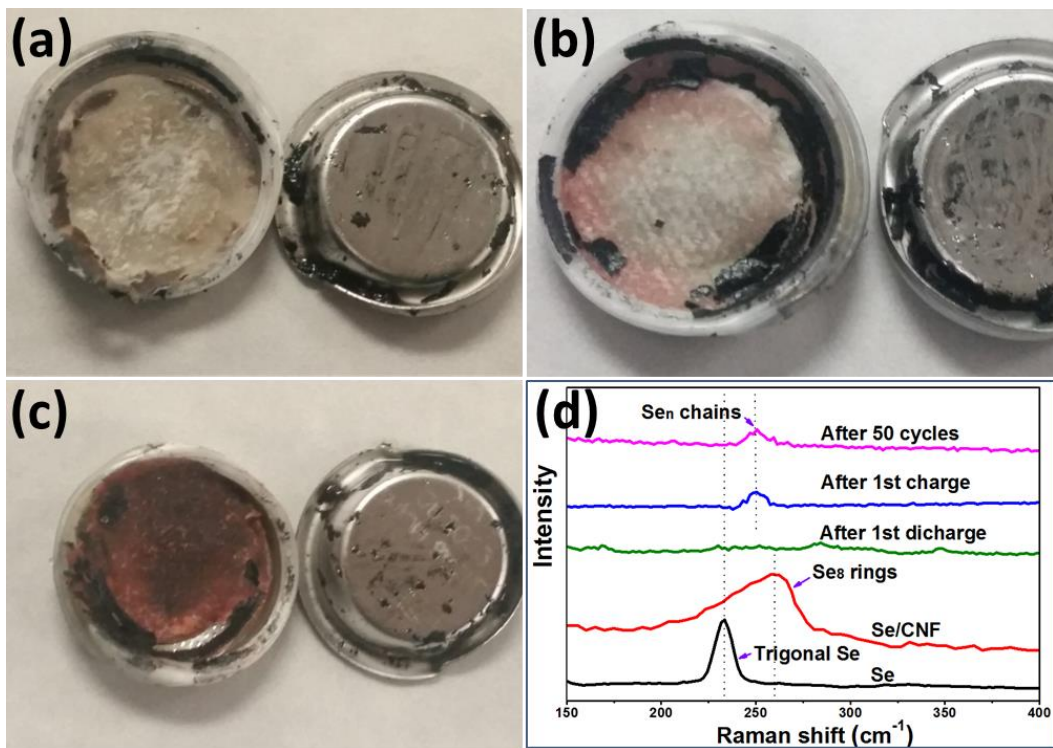


**Figure S11.** Photographs of the (a) carbon-coated glass fiber (carbon coating was stripped off when the image was taken) and (b) pure glass fiber separator facing the CNF/Se electrode (prepared at 260 °C). (c) Photographs of the pure glass separator facing the CNF/Se electrode (prepared at 110 °C). (d) Raman spectrum of the cycled CNF/Se electrode.

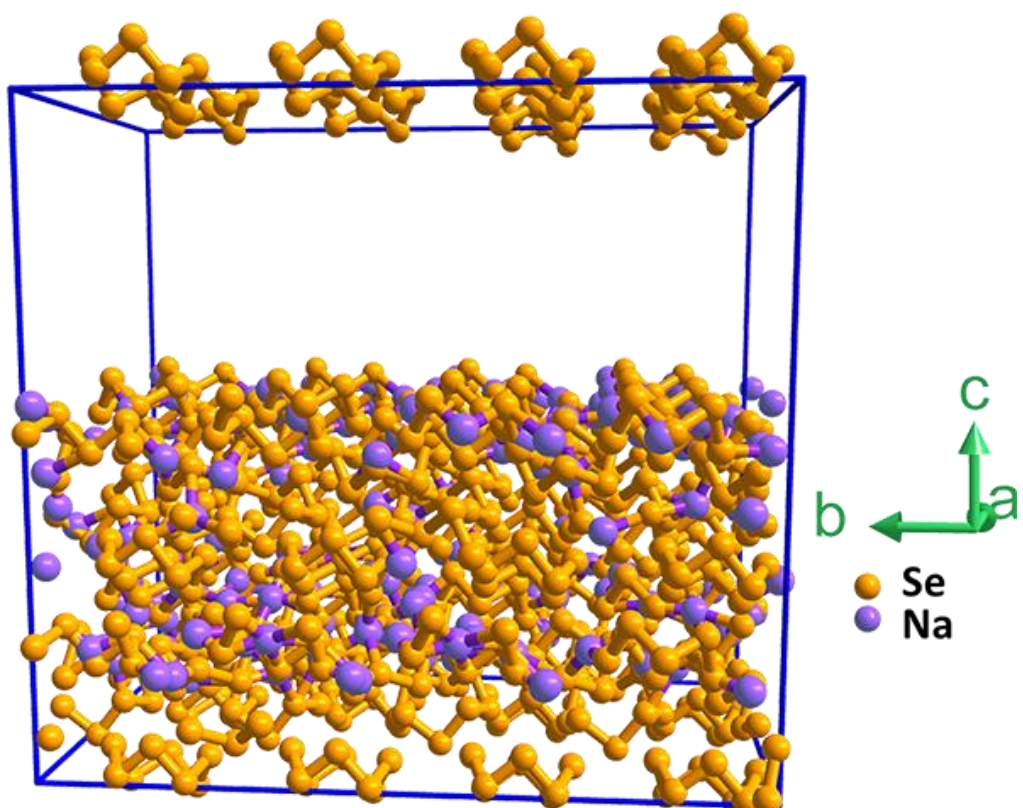


**Figure S12.** Final structure obtained by the MD simulations, which contains 512 Se atoms and 139 Na atoms.

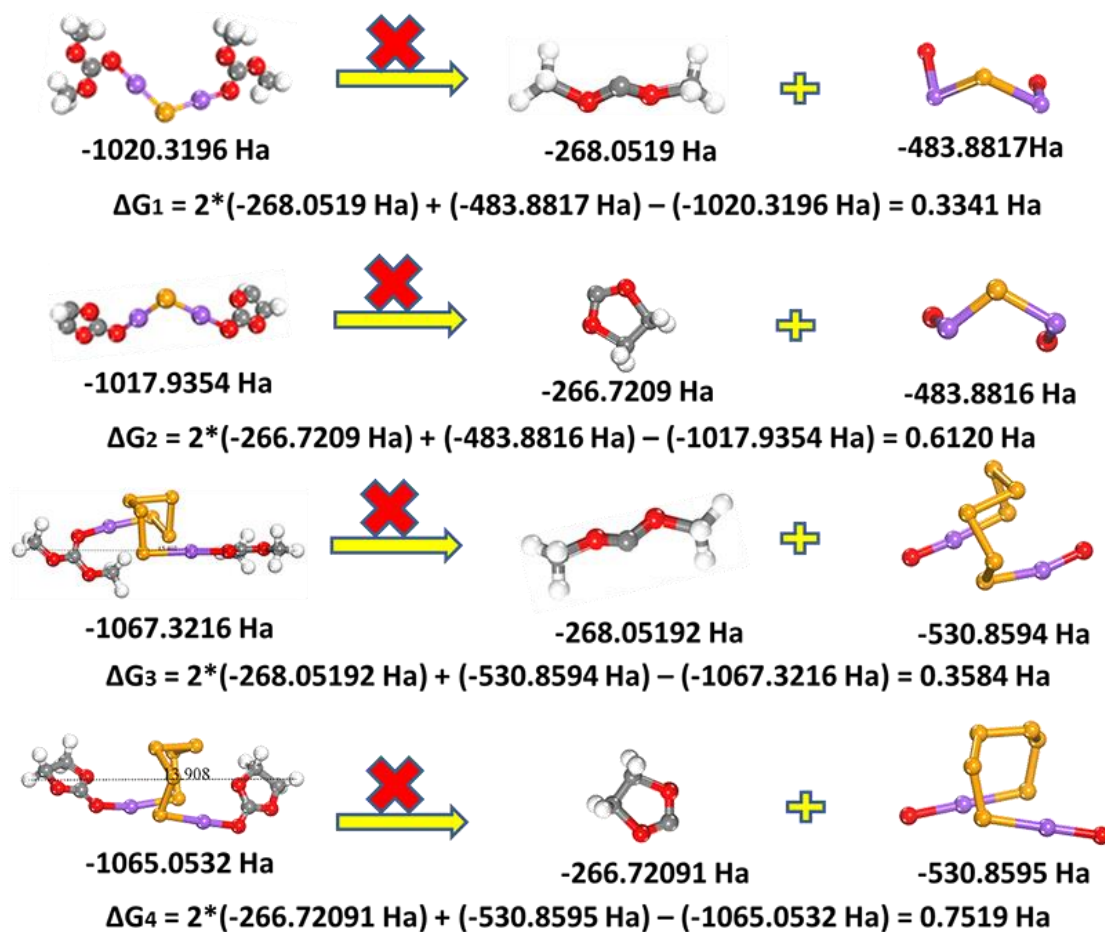


**Figure S13.** Theoretical calculation results of the energy of  $\text{Na}_2\text{Se-EC}$ ,  $\text{Na}_2\text{Se-DMC}$ ,  $\text{DMC}$ ,  $\text{Na}_2\text{Se}_6\text{-DMC}$ ,  $\text{Na}_2\text{Se}_6\text{-EC}$ ,  $\text{Na}_2\text{SeO}_2$ ,  $\text{Na}_2\text{Se}_6\text{O}_2$ , and the broken pieces of  $\text{EC}$ ,  $\text{DMC}$ .

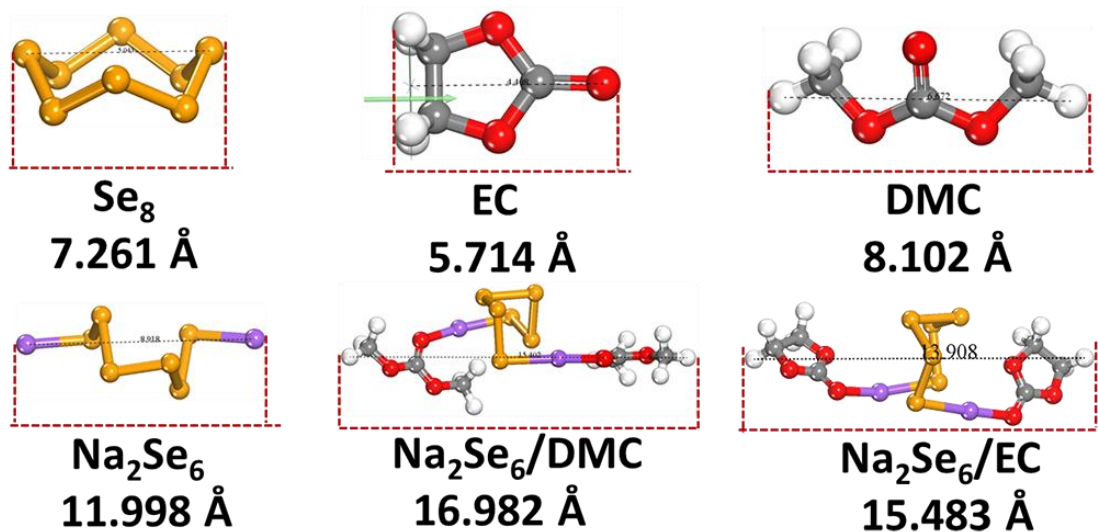


**Figure S14.** Theoretical calculation results of  $\text{Se}_8$ , EC, DMC,  $\text{Na}_2\text{Se}_6$ ,  $\text{Na}_2\text{Se}_6$ -DMC,  $\text{Na}_2\text{Se}_6$ -EC.

**Table S1** Summary of the representative selenium-based cathode materials for SIBs

Materials	Selenium wt. % (loading: mg cm <sup>-2</sup> )	Reversible specific capacity	Cycling performance	References
<b>Carbon-Selenium composites</b>	54(1.2)	595 mA h g <sup>-1</sup> at 50 mA g <sup>-1</sup>	42.6% retention over 50 cycles	[5]
<b>Selenium-mesoporous carbon</b>	30(-)	485 mA h g <sup>-1</sup> at 169.5 mA g <sup>-1</sup>	70% retention over 380 cycles	[39]
<b>Se/CNF-CNT</b>	35(2)	590 mA h g <sup>-1</sup> at 50 mA g <sup>-1</sup>	98% retention over 80 cycles	[6]
<b>CPAN/Se fibers</b>	36(-)	490 mA h g <sup>-1</sup> at 67.8 mA g <sup>-1</sup>	81% retention over 300 cycles	[40]
<b>Se-PAN derived carbon nanofibers</b>	52(0.8)	595 mA h g <sup>-1</sup> at 100 mA g <sup>-1</sup>	87% retention over 80 cycles	[41]
<b>Se-porous carbon</b>	57.6(-)	624 mA h g <sup>-1</sup> at 67.8 mA g <sup>-1</sup>	84% retention over 150 cycles	[38]
<b>Se-CCN</b>	53 (2)	613 mA h g <sup>-1</sup> at 67.8 mA g <sup>-1</sup>	88% retention over 500 cycles	[37]
<b>Se-Carbon with Slit micropores</b>	50.2(2)	596 mA h g <sup>-1</sup> at 67.8 mA g <sup>-1</sup>	88% retention over 100 cycles	[34]
<b>CNF/Se composite and C-coated separator</b>	72.1(4.4)	599 mA h g <sup>-1</sup> at 67.8 mA g <sup>-1</sup>	85.6% retention over 120 cycles	This work

- [1] Qie, L., A. Manthiram, *Adv. Mater.* **2015**, *27*, 1694.
- [2] Blöchl, P.E., *Phys. Rev. B* **1994**, *50*, 17953.
- [3] Perdew, J.P., W. Yue, *Phys. Rev. B* **1986**, *33*, 8800.
- [4] Grimme, S., *J. Comput. Chem.* **2006**, *27*, 1787.
- [5] Luo, C., J. Wang, L. Suo, J. Mao, X. Fan, C. Wang, *J. Mater. Chem. A* **2014**, *3*, 555.
- [6] Zeng, L., X. Wei, J. Wang, Y. Jiang, W. Li, Y. Yu, *J. Power Sources* **2015**, *281*, 461.